

Intraseasonal variability of air-sea fluxes over the Bay of Bengal during the southwest monsoon

Article

Accepted Version

Sanchez-Franks, A., Kent, E. C., Matthews, A. J., Webber, B. G. M., Peatman, S. C. and Vinayachandran, P. N. (2018) Intraseasonal variability of air-sea fluxes over the Bay of Bengal during the southwest monsoon. *Journal of Climate*, 31 (17). pp. 7087-7109. ISSN 1520-0442 doi: <https://doi.org/10.1175/JCLI-D-17-0652.1> Available at <https://centaur.reading.ac.uk/77492/>

It is advisable to refer to the publisher's version if you intend to cite from the work. See [Guidance on citing](#).

To link to this article DOI: <http://dx.doi.org/10.1175/JCLI-D-17-0652.1>

Publisher: American Meteorological Society

All outputs in CentAUR are protected by Intellectual Property Rights law, including copyright law. Copyright and IPR is retained by the creators or other copyright holders. Terms and conditions for use of this material are defined in the [End User Agreement](#).

www.reading.ac.uk/centaur

CentAUR

Central Archive at the University of Reading

Reading's research outputs online

1 **Intraseasonal Variability of Air-Sea Fluxes over the Bay of Bengal during**
2 **the Southwest Monsoon**

3 Alejandra Sanchez-Franks*, Elizabeth C. Kent

4 *National Oceanography Centre, Southampton, UK*

5 Adrian J. Matthews, Benjamin G. M. Webber

6 *Centre for Ocean and Atmospheric Sciences, School of Environmental Sciences, University of*
7 *East Anglia, Norwich, UK*

8 Simon C. Peatman

9 *National Centre for Atmospheric Science - Climate, University of Reading, UK*

10 P. N. Vinayachandran

11 *Centre for Atmospheric and Oceanic Sciences, Indian Institute of Science, Bangalore, India*

12 *Corresponding author address: A. Sanchez-Franks, National Oceanography Centre, European

13 Way, Southampton, UK, SO14 3ZH

14 E-mail: alsf@noc.ac.uk

ABSTRACT

15 In the Bay of Bengal (BoB), surface heat fluxes play a key role in monsoon
16 dynamics and prediction. The accurate representation of large-scale surface
17 fluxes is dependent on the quality of gridded reanalysis products. Meteorological
18 and surface flux variables from five reanalysis products are compared
19 and evaluated against in situ data from the RAMA moored array in the BoB.
20 The reanalysis products: ERA-Interim (ERA-I), TropFlux, MERRA-2, JRA-
21 55 and CFSR are assessed for their characterisation of air-sea fluxes during
22 the southwest monsoon season (JJAS). ERA-I captured radiative fluxes best
23 while TropFlux captured turbulent and net heat fluxes (Q_{net}) best, and both
24 products outperformed JRA-55, MERRA-2 and CFSR, showing highest correlations
25 and smallest biases when compared to the in situ data. In all five
26 products, the largest errors were in shortwave radiation (Q_{SW}) and latent heat
27 flux (Q_{LH}), with non-negligible biases up to $\sim 75 \text{ W m}^{-2}$. The Q_{SW} and Q_{LH}
28 are the largest drivers of the observed Q_{net} variability, thus highlighting the
29 importance of the results from the buoy comparison. There are also spatially
30 coherent differences in the mean basin-wide fields of surface flux variables
31 from the reanalysis products, indicating that the biases at the buoy position are
32 not localized. Biases of this magnitude have severe implications on reanalysis
33 products ability to capture the variability of monsoon processes. Hence, the
34 representation of intraseasonal variability was investigated through the boreal
35 summer intraseasonal oscillation and we found that TropFlux and ERA-I perform
36 best at capturing intraseasonal climate variability during the southwest
37 monsoon season.

38 **1. Introduction**

39 Circulation in the Indian Ocean is governed by monsoon variability (Lau et al. 2012; Weller
40 et al. 2016). In the Bay of Bengal (BoB), sea surface temperature (SST) and heat flux are the
41 key components in southwest (SW) monsoon behavior (Vecchi and Harrison 2002; Parampil et al.
42 2010; Vialard et al. 2011). The mechanism via which the surface net heat fluxes (Q_{net}) impact
43 SST variability is linked to the BoB barrier layer (Duncan and Han 2009). During the summer,
44 a combination of increased precipitation and river runoff in the northern BoB contributes to the
45 formation of a highly stratified surface barrier layer that sits above the thermocline and below the
46 mixed layer base (Vinayachandran et al. 2002). The summer barrier layer acts to inhibit processes
47 such as entrainment, vertical advection and upwelling, which result in surface Q_{net} having a greater
48 impact on the intraseasonal SST variability (Duncan and Han 2009).

49 The importance of the Q_{net} as a driver of summer SST variability in the BoB (Duncan and Han
50 2009; Lau et al. 2012) is also shown in observations and ocean models, where summer intrasea-
51 sonal oscillations (ISO) of SST are forced mainly by heat flux variability, with occasional contri-
52 butions from vertical mixing and entrainment at the base of the mixed layer (Schiller and Godfrey
53 2003; Waliser 2006; Girishkumar et al. 2017). Both models and observations indicate that the
54 intraseasonal oscillation of the northern Indian Ocean SST impacts the large-scale atmospheric
55 wind field, temperature, humidity and the active–break cycle of monsoon convection (Vecchi and
56 Harrison 2002; Waliser 2006; Yang et al. 2008). Studies suggest that fluctuations in SST, driven
57 by surface heat fluxes (Q_{net}), can be used as an indicator/proxy for the forecast of active and break
58 periods in the monsoon (Vecchi and Harrison 2002; Parampil et al. 2010). Consequently, the accu-
59 rate measurement and representation of SST and Q_{net} are critical in understanding and predicting

60 SW monsoon processes over the BoB (Vialard et al. 2011), and monsoon variability and dynamics
61 (Vecchi and Harrison 2002).

62 Several studies have reported significant differences between flux products and in situ data in
63 the Indian Ocean (e.g., Yu et al. 2007; McPhaden et al. 2009; Kumar et al. 2012; Goswami et al.
64 2014; Weller et al. 2016). McPhaden et al. (2009) found that then-current numerical weather pre-
65 diction (NWP) products underestimated Q_{net} by 40-60 $W m^{-2}$ compared with in situ estimates
66 from a moored buoy near $0^\circ, 80.5^\circ E$. Their results suggested that the accumulation of these defi-
67 ciencies in heat flux over time could result in $2^\circ C$ errors in SST . Kumar et al. (2012) compared
68 reanalysis products with moored buoy data in the global tropical oceans to create a blended flux
69 product, TropFlux, which is based on fields from the best performing product: the European Centre
70 for Medium-Range Weather Forecasts (ECMWF) ERA-Interim (ERA-I) (Dee et al. 2011). They
71 found that older reanalyses had larger biases and rms differences than ERA-I when compared to
72 the in situ data. Yu et al. (2007) compared NWP, reanalysis and blended products for annual, sea-
73 sonal and interannual time scales in the Indian Ocean and found differences between 53 and 108
74 $W m^{-2}$ for daily averaged measurements. Goswami et al. (2014) showed that the coupled Climate
75 Forecast System Reanalysis (CFSR) product does not accurately simulate monsoon intraseasonal
76 variability. These studies highlight significant shortcomings with reanalysis fields in the Indian
77 Ocean and suggest that the accumulated errors found in reanalysis and blended products could
78 lead to significant deficiencies in their representation of Indian Ocean processes.

79 To determine whether any reanalysis product gives a robust representation of monsoon pro-
80 cesses, particularly in the BoB, it is important to understand their individual performance in rep-
81 resenting air-sea fluxes and related meteorological parameters, such as SST , surface wind speed
82 (V), air temperature (T_a), and specific humidity (q_a). The products examined in this work include
83 the atmospheric global reanalysis products: ERA-I (Dee et al. 2011), the National Aeronautics

84 and Space Administrations (NASA) Modern Era Retrospective-Analysis for Research and Ap-
85 plications v2 (MERRA-2) (Rienecker et al. 2011), the Japanese Meteorological Agency (JMA)
86 Japanese 55-year Reanalysis (JRA-55) (Kobayashi et al. 2015), the National Centers for Envi-
87 ronmental Prediction (NCEP) CFSR (Saha et al. 2010), and the air-sea flux product focused on
88 the tropical oceans, TropFlux (Kumar et al. 2012). The products are assessed using in situ data
89 from the Research Moored Array for African-Asian-Australian Monsoon Analysis and Prediction
90 (RAMA) (McPhaden et al. 2009). The BoB is a region where monsoon processes are still not fully
91 understood (Weller et al. 2016) and in situ data are sparse (Vinayachandran et al. 2018), making
92 gridded reanalysis products hard to verify.

93 Section 2 gives a brief overview of the datasets used in this paper, including four reanalysis
94 products, a blended product, and in situ data. The analysis and discussion of air-sea fluxes in the
95 BoB for the SW monsoon season (JJAS) is presented in sections 3, 4 and 5. There is a comparison
96 of reanalysis products with in situ data from RAMA buoys in the BoB for interannual variability
97 (section 3), an in-depth analysis of individual flux components (section 4), and an evaluation of the
98 reanalysis products characterisation of basin-wide air-sea fluxes and the associated intraseasonal
99 variability from the boreal summer intraseasonal oscillation (section 5). A summary is given in
100 section 6.

101 **2. Data and Methods**

102 The characterisation of air-sea fluxes in the BoB from flux products is investigated using mete-
103 orological (SST, V , T_a , q_a) and flux parameters [shortwave radiation (Q_{SW}), longwave radiation
104 (Q_{LW}), sensible heat flux (Q_{SH}), latent heat flux (Q_{LH}) and Q_{net}] from four reanalysis products,
105 one blended product, and in situ data from the RAMA moored array. The surface fluxes from the
106 reanalysis products are model fluxes, turbulent fluxes for RAMA and TropFlux are calculated from

107 meteorological parameters following Fairall et al. (2003), radiative fluxes are measured by RAMA
 108 and derived as described in Kumar et al. (2012) for TropFlux. In all reanalysis (and blended)
 109 datasets, T_a and q_a are provided at 2 m height above sea level, and V is provided at 10 m. The in
 110 situ buoy data measures T_a and q_a at 3 m, and V at 4 m, which are adjusted to 2 m and 10 m re-
 111 spectively using COARE v3.0 algorithm (Fairall et al. 2003). Note, q_a is not available from ERA-I
 112 or at the RAMA sites. Instead, we use dewpoint temperature from ERA-I and relative humidity
 113 in the case of RAMA, from which we derive the vapour pressure (e) and thus calculate q_a , as per
 114 Bolton (1980):

$$q_a = \left[\epsilon \frac{e}{p - e(1 - \epsilon)} \right] \times 1000 \quad (1)$$

115 where p is surface pressure and $\epsilon = 0.622$ is the ratio of the molecular masses of water vapour
 116 and dry air. Similarly the specific humidity at the sea surface, q_s , is computed from SST as per
 117 equation (1), where the saturation specific humidity is assumed to be at 98% saturation at the SST .

118 Data were obtained at the temporal resolutions described in section 2a for the summer periods
 119 (JJAS) from 2007 to 2015 and then daily averaged, as daily resolution is adequate for resolving
 120 intraseasonal variability which is the primary mode of variability for monsoonal processes. In
 121 the following sections, both meteorological and flux variables from the reanalysis data have been
 122 regrided to $1^\circ \times 1^\circ$, by linear interpolation, where necessary. The data products used in this paper
 123 are briefly described here and in Table 1.

124 *a. Reanalysis and blended products*

125 ERA-I is a global atmospheric reanalysis product from the ECMWF (Dee et al. 2011). The ERA-
 126 I data assimilation system uses 4-dimensional variational analysis (4D Var), with an improved
 127 hydrological cycle and quality control compared with the previous ECMWF reanalysis product:
 128 ERA-40 (Berrisford et al. 2011). The mean state variables used here are from the analysis field

129 (step 0) at 6-hourly time intervals and the flux variables are from the forecast field (step 12) at
130 3-hourly time intervals. All variables are obtained on a $1^\circ \times 1^\circ$ horizontal grid.

131 TropFlux is a blended (reanalysis-based) product of air-sea fluxes and associated meteorological
132 variables over the global tropical oceans, from 30°S to 30°N (Kumar et al. 2012, hereafter KP12).
133 TropFlux uses ISCCP satellite cloud data (Zhang et al. 2004) to compute Q_{SW} , and bias-adjusted
134 ERA-I (Dee and Uppala 2009) data to compute SST , V , T_a , q_a and Q_{LW} as per:

$$\Psi_{tf}(x,y,t) = a(\Psi(x,y,t) - \bar{\Psi}(x,y)) + b(x,y) + \bar{\Psi}(x,y) \quad (2)$$

135 where Ψ_{tf} is the corrected ERA-I variable, Ψ , and the long term mean is $\bar{\Psi}$. The amplitude, a , and
136 bias, b , adjustments of the TropFlux variables are based on a comparison between the reanalysis
137 product and in situ data from the Global Tropical Moored Buoy Array (McPhaden 2010). The
138 turbulent fluxes were computed using the COARE v3.0 algorithm (Fairall et al. 2003) on the
139 corrected daily-averaged input variables and, since TropFlux computes heat fluxes from daily
140 averaged data, a gustiness correction is applied to the surface wind speed parameter to compensate
141 for the higher frequency (< 1 day) fluctuations in wind speed, which result in underestimations
142 in the flux variability based on results of Cronin et al. (2006). The cool skin and warm layer
143 calculations in COARE v3.0 are switched off (Kumar et al. 2012). The gustiness correction is
144 applied to the surface wind speed parameter only for the computation of turbulent heat fluxes. The
145 TropFlux data are served as daily means, on a $1^\circ \times 1^\circ$ horizontal grid. The spatially homogeneous
146 amplitude adjustment (a) acts to increase the variance of all the parameters in ERA-I around
147 their long term values. We note that TropFlux adjusts ERA-I meteorological parameters based
148 on measurements from the Global Tropical Moored Buoy Array, however, only data to the end
149 of 2009 was available at the time TropFlux was produced. At this time the RAMA array had
150 only recently been established: measurements at b28 started in November 2006, with b26 and

151 b27 being added a year later. The observational constraints will therefore be dominated by the
152 longer-established moorings in the Pacific, and to a lesser extent, in the Atlantic.

153 JRA-55 is the second global atmospheric reanalysis product produced by the JMA (Kobayashi
154 et al. 2015), built to improve upon JRA-25 (Onogi et al. 2007). JRA-55 has a new longwave
155 radiation scheme, increased spatial resolution, and uses variational bias correction (VarBC) and
156 4D Var analysis. The data used here are on a $0.56^\circ \times 0.56^\circ$ grid using analysis fields for the mean
157 state variables and 3-hourly averages for the flux variables.

158 MERRA-2 is a global atmospheric reanalysis of the satellite period produced by NASA
159 (Bosilovich et al. 2015), and updated from the original MERRA product (Rienecker et al. 2011).
160 MERRA-2 uses an updated atmospheric data assimilation system: the Goddard Earth Observing
161 System (GEOS-5) with a 3D Var algorithm. Important updates to MERRA-2 since the origi-
162 nal MERRA product also include an updated observing system with more satellite observations,
163 and an aerosol analysis (Bosilovich et al. 2015). The MERRA-2 data has a spatial resolution of
164 0.5° latitude by 0.625° longitude on 72 levels. Here, the mean state variables are at 1-hourly, in-
165 stantaneous, single-level diagnostics and the flux variables are 1-hourly, time-averaged, radiation
166 diagnostics.

167 CFSR is a coupled ocean-atmosphere reanalysis product created by the NCEP (Saha et al. 2010).
168 The Coupled Forecast System model that CFSR uses includes a spectral atmospheric model and
169 the Modular Ocean Model from the Geophysical Fluid Dynamics Laboratory. The atmospheric
170 model has a spatial resolution of $0.5^\circ \times 0.5^\circ$ on 37 vertical levels, and the ocean model has a
171 resolution of 0.5° on 40 vertical levels. CFSR was completed for the period of 1979 to 2009
172 and was later extended to 2011. In 2011, CFSv2 was implemented as a continuation of CFSR
173 (Saha et al. 2011). As CFSv2 uses the same model as CFSR, the CFSv2 product is treated as
174 an extension of CFSR and CFSv2 is hereafter implied in any mention of CFSR. The data were

175 available at 6-hour forecast field for mean state variables and at 6-hour averaged field for flux
176 variables.

177 All reanalysis products assimilate ocean observations from fixed mooring arrays, including the
178 Global Tropical Moored Array (McPhaden 2010).

179 *b. In situ data: the RAMA array*

180 RAMA is an array of moored buoys in the Indian Ocean that provide atmospheric and oceano-
181 graphic data for the study of ocean circulation, air-sea interactions and monsoon dynamics
182 (McPhaden et al. 2009). The types of moored buoys relevant for this study within the RAMA
183 network are the surface and enhanced surface moorings. The enhanced surface moorings are Au-
184 tonomous Temperature Line Acquisition System (ATLAS) moorings with additional sensors for
185 pressure and longwave radiation measurements designed for measuring complete air-sea interac-
186 tions, and are denominated flux reference sites. In the BoB, there are two surface moorings located
187 at 8°N, 90°E (designated b26) and 12°N, 90°E (b27), and one enhanced surface mooring at 15°N,
188 90°E (b28).

189 Meteorological variables used include SST (measured at 1 m below sea surface), V (measured
190 at 4 m above sea surface and converted to 10 m height by the data providers), T_a (measured
191 at 3 m above sea surface and adjusted to 2 m), and relative humidity (measured at 3 m above
192 sea surface and adjusted to 2 m), T_a and pressure from which q_a is computed as per equation
193 (1). All height adjustments use the COARE v3.0 algorithm as per Fairall et al. (2003). Table
194 2 shows the uncertainties for the meteorological variables (SST , V , T_a , humidity), which corre-
195 spond to the Next Generation ATLAS Mooring Sensors accuracies listed on the NOAA/PMEL
196 website, <https://www.pmel.noaa.gov/gtmba/sensor-specifications>. These accuracies are based on

197 calibrations for pre-deployment and post-recovery. ΔT and Δq uncertainties are calculated using
198 quadrature (Table 2).

199 The air-sea flux variables are computed using the COARE 3.0b algorithm (Fairall et al. 2003;
200 Cronin et al. 2006) by data providers. Net radiative fluxes, also calculated by providers, were
201 calculated from measured downwelling components following Cronin et al. (2006) such that:

$$Q_{SW} = (1 - \alpha) \times SWR \quad (3)$$

202

$$Q_{LW} = \varepsilon(\beta \times T_s^4 - LWR) \quad (4)$$

203 where α is a constant albedo value of 0.055, SWR is the incoming downwelling radiation, ε
204 is the emissivity constant (0.97), β is the Stefan Boltzman constant (5.67×10^{-8}), T_s is the skin
205 temperature (K) and LWR is the incoming downwelling longwave radiation. For the turbulent
206 fluxes, biases from daily resolved wind speed in the RAMA fluxes (computed using COARE 3.0)
207 are minimized by applying a gustiness correction in the wind speeds prior to their use in the bulk
208 flux calculations as per Cronin et al. (2006). We estimated the turbulent flux uncertainties (Table
209 2) from the standard deviation of differences between RAMA turbulent fluxes (calculated using
210 hourly data input for the COARE3.0 algorithm, including cool skin and warm layer effects) and
211 turbulent fluxes estimated from RAMA meteorological variables perturbed with the instrument
212 uncertainties (input data was daily averaged in the COARE3.0 algorithm, and as per Cronin et al.
213 (2006) cool skin and warm layer effects were turned off). We note that there is a mean difference
214 of 0.13 and 2.25 W m^{-2} for Q_{SH} and Q_{LH} respectively when comparing turbulent fluxes estimated
215 from hourly averaged data (cool skin and warm layer effects turned on) and daily averaged data
216 (cool skin and warm layer turned off). Subsets of RAMA data can be obtained from the TAO
217 Project Office of NOAA/PMEL, where meteorological and flux variables are available at high (up

218 to 10 min) resolution. All meteorological and flux variables are presented in this paper averaged
219 to give daily resolution.

220 The RAMA moorings in the BoB have been operational since 2007; however, issues in buoy
221 maintenance affect data return resulting in intermittent data coverage (McPhaden 2010). Fig. 1
222 shows the availability of parameters used in this study at b28. As b27 and b26 are not flux reference
223 sites, pressure (hence q_a) and Q_{LW} are not available at these buoy locations (not shown here).
224 The most comprehensive coverage occurs at site b28, with almost complete data return in *SST*.
225 Noticeable gaps for the remaining variables occur mostly during 2007, 2008, 2011, 2012 and (for
226 *V* and turbulent fluxes only) 2013. Due to the data limitation at sites b27 and b26, the following
227 time series analysis using reanalysis products and the RAMA buoys will focus only on data from
228 site b28.

229 3. Evaluation of meteorological and flux variables

230 In this section, the five data products are evaluated against in situ data from the RAMA buoy b28
231 in the BoB for the summer months (JJAS), from 2007 to 2015. We evaluate the meteorological
232 parameters important for calculation of turbulent fluxes: *SST*, *V*, T_a and q_a , as well as the air-
233 sea temperature difference, ΔT , the air-sea humidity difference, Δq , the turbulent fluxes, Q_{SH} and
234 Q_{LH} , the radiative fluxes, Q_{SW} and Q_{LW} , and the Q_{net} . In the following section, meteorological
235 variables are further investigated to understand their impact on the turbulent fluxes in this region
236 and the causes for disparities in the products' ability to represent surface fluxes.

237 Individual daily values of the surface fluxes and associated variables for each of the products are
238 compared to RAMA b28 using four metrics. Firstly the differences (product - b28) and their 95%
239 confidence intervals (calculated using a t test implemented in R using function `t.test` (R Core Team
240 2015)) are presented (Fig. 2a). Second, the Pearson product moment correlation coefficients for

241 each product with b28 and their 95% confidence intervals (calculated in R using function cor.test)
 242 are presented (Fig. 2b). Fig. 2c shows the variance ratio of the parameters with their 95% confi-
 243 dence interval (calculated using an F test implemented in R using function var.test). Fig. 2d com-
 244 bines these metrics to give skill scores for each product and variable (Wallcraft et al. 2009). Skill
 245 scores are an established way to assess the quality of numerical weather forecasts (Murphy 1988)
 246 and are based on the correlation between the product being assessed and a reference standard,
 247 penalized for disagreement in mean values and variance ratio. Thus, if we denote x_i ($i = 1, \dots, n$)
 248 as the observations and y_i ($i = 1, \dots, n$) as a data product for a sample of n , we can define the linear
 249 correlation, R , and skill score, SS , between x_i and y_i as per Murphy (1988):

$$R = \frac{1}{n} \sum_{i=1}^n \frac{(x_i - \bar{\mathbf{x}})(y_i - \bar{\mathbf{y}})}{(\sigma_x \sigma_y)} \quad (5)$$

$$SS = R^2 - \left[R - \frac{\sigma_y}{\sigma_x} \right]^2 - \left[\frac{(\bar{\mathbf{y}} - \bar{\mathbf{x}})}{\sigma_x} \right]^2 \quad (6)$$

251 where $\bar{\mathbf{x}}$, $\bar{\mathbf{y}}$ and σ_x , σ_y are the sample mean and standard deviation of x_i and y_i , respectively.
 252 Skill scores of 1 demonstrate perfect agreement between the data products and the observed data.
 253 Perfectly correlated data with a 25% underestimate of variance and a bias of magnitude of 25% of
 254 the variance would have a skill score of 0.5. Negative skill scores typically arose in our comparison
 255 due to substantial underestimates of variance combined with large mean differences, although
 256 there were also some low correlation values.

257 *Sea surface temperature* For *SST*, all reanalysis products show fairly strong correlations with
 258 RAMA b28 (Fig. 2b). ERA-I shows the largest offset (-0.37 °C), followed by MERRA-2 (-
 259 0.20 °C), both underestimating the in situ *SST* (Fig. 2a). Both these reanalyses use the OSTIA
 260 foundation *SST* product (Donlon et al. 2012) in the period of our analysis so are expected to
 261 have colder *SST*s than a standard near-surface estimate. MERRA-2 uses OSTIA after 2006 and
 262 ERA-I from February 2009, The reason for the difference between the *SST* for these products is

263 therefore not clear; their agreement improves from 2009 but remains $0.2\text{ }^{\circ}\text{C}$ (not shown). JRA-55
264 *SST* agrees well with b28, with the smallest bias and highest correlation (Fig. 2b, 0.90), giving
265 the highest skill in reproducing the b28 *SST* (Fig. 2d), despite an underestimate of the variance
266 (Fig. 2c). The coupled product CFSR also shows a good representation of the observed *SST*.
267 We note that the CFSR *SST* is constrained through a relaxation coefficient at the sea surface (i.e.
268 model *SST* is nudged toward observed *SST*), which counteracts any drift in the model related to
269 error in the surface fluxes (Xue et al. 2011). On the other hand, JRA-55, MERRA-2, and ERA-I
270 are atmosphere-only reanalysis products with prescribed *SST* fields (Table 1).

271 *Surface wind speed* V shows the highest correlation (≥ 0.9) across all products with V from
272 RAMA b28. TropFlux and MERRA-2 V are closest to that from b28. ERA-I and JRA-55 under-
273 estimate and CFSR overestimates the observed V (Fig. 2a). Variance ratios are around one, apart
274 from CFSR, which shows significantly greater variance in V than b28 (Fig. 2c). V shows the best
275 skill scores across the variables with ERA-I, TropFlux and JRA all having skill scores of about
276 0.9 (Fig. 2d).

277 *Air Temperature* The highest T_a correlations are observed with ERA-I, TropFlux and JRA-55
278 (≥ 0.83) and the lowest correlation with MERRA-2 (0.62) (Fig. 2b). ERA-I has the largest offset
279 ($-0.38\text{ }^{\circ}\text{C}$), the other products are within $0.1\text{ }^{\circ}\text{C}$ of b28 (Fig. 2a). TropFlux significantly overes-
280 timates the variance, and MERRA-2 and CFSR significantly underestimate the variance (Fig. 2c).
281 Overall JRA-55 shows the best skill, followed by TropFlux (Fig. 2d).

282 *Specific humidity* The products all struggle with reproducing the observed q_a . Kumar et al.
283 (2012) found that ERA-I underestimated q_a , and attributed more than half of that estimate to a
284 cold bias in T_a and the remainder to an underestimate in the relative humidity. However their
285 adjustment to q_a for ERA-I for TropFlux results in an overestimate at b28. Skill scores are all

286 less than 0.2, resulting from a combination of modest correlations (< 0.8), large mean biases
287 ($> 0.3 \text{ g kg}^{-1}$), and a large underestimate of the variance. Our results show a CFSR dry bias
288 also previously observed in the maritime continent and western Pacific by Wang et al. (2011) and
289 overall dry bias found in ERA-I when compared to research vessel data (Brunke et al. 2011).

290 *Air-sea temperature difference* For all products except ERA-I, the skill scores for ΔT are much
291 lower than those for either SST or T_a (Fig. 2d). JRA-55 performs best, combining a small bias
292 (Fig. 2a) with the strongest correlation (Fig. 2b) and is the only product to make a reasonable
293 estimate of the variance (Fig. 2c).

294 *Air-sea humidity difference* The skill scores for Δq for ERA-I, JRA-55 and MERRA-2 are larger
295 than their respective skill scores for q_a , but the best skill score is only 0.5 for MERRA-2 (Fig. 2d).
296 Modest correlations combined with large biases for most products (Fig. 2a) and a very significant
297 underestimate of variance (Fig. 2c) give poor skill overall.

298 *Shortwave radiation* For all products apart from TropFlux, biases in Q_{SW} (and Q_{LW}) are di-
299 rectly linked to its radiation schemes, spatial distribution and aerosol properties (Dee et al. 2011).
300 TropFlux Q_{SW} uses observed cloudiness data from ISCCP up until the end of 2007 (when it was
301 last available), and the ISCCP mean seasonal cycle and adjusted using NOAA outgoing longwave
302 radiation (OLR) thereafter (KP12). TropFlux and ERA-I show the highest correlations (~ 0.7)
303 with the observed Q_{SW} (Fig. 2b) and the highest overall skill (Fig. 2d). All of the products un-
304 derestimate Q_{SW} apart from CFSR which overestimates by more than 70 W m^{-2} . MERRA-2 and
305 CFSR show the lowest correlations (Fig. 2b) and highest biases (Fig. 2a). Positive bias in CFSR
306 Q_{SW} in the tropics has been previously catalogued by Wang et al. (2011) due to an underestimate
307 of cloudiness. MERRA-2s underestimation of Q_{SW} has been similarly linked to its cloud scheme

308 (general difficulties capturing irradiance variability) in a study by Boilley and Wald (2015). All of
309 the products significantly underestimate the variability of Q_{SW} (Fig. 2c).

310 *Longwave radiation* The skill scores for Q_{LW} are very low, with only ERA-I achieving a positive
311 score (Fig. 2d). All products underestimate the variance (Fig. 2c) and for all of the products other
312 than ERA-I the biases are large relative to the variability resulting in low skill.

313 *Sensible heat flux* TropFlux has the most skill due to a relatively high correlation of 0.79, a small
314 bias of slightly over 1 W m^{-2} but overestimates the variance. ERA-I and JRA-55 have negative
315 skill scores due to large biases and overestimates of variance. The poor skill in JRA-55 is hard to
316 understand as it performed best at reproducing ΔT and showed high skill for V .

317 *Latent heat flux* TropFlux is the only product to have a positive skill score for Q_{LH} . This is sur-
318 prising as it had relatively poor skill for Δq (Fig. 2d). TropFlux underestimates Δq but shows only
319 a small underestimate in Q_{LH} which may indicate that the gustiness parameter used by TropFlux
320 in the transfer coefficients may be acting to compensate for low Δq with an enhanced wind effect
321 in the flux calculation. MERRA-2s large overestimation of Q_{LH} can be attributed to the fact that
322 MERRA-2 has humidity (dry) bias problems related to forecast model spin up/down (Kobayashi
323 et al. 2015). The large Q_{LH} bias apparent in CFSR has been observed on a global scale (larger
324 evaporative cooling, in general) and is linked to the dry bias over the equatorial Indian Ocean
325 (Wang et al. 2011) and the erroneously strong winds (Fig. 2a).

326 *Net heat flux* TropFlux has the highest skill in reproducing Q_{net} . CFSR does better than expected,
327 despite having negative skill scores for 3 of the 4 flux components, and ERA-I is the only other
328 product to have a positive skill score (Fig. 2d). ERA-I, JRA-55 and MERRA-2 all have too much
329 heat loss from the ocean. TropFlux and CFSR all show a mean net heat gain by the ocean of
330 $30\text{-}35 \text{ W m}^{-2}$ over JJAS of 2007-2015, whereas ERA-I, JRA-55 and MERRA-2 all show a net

331 heat loss of between -20 to -50 W m^{-2} (not shown here). We note that biases in turbulent and
332 radiative fluxes cancel out in the Q_{net} from CFSR and (to a smaller degree) TropFlux. However,
333 biases (mostly) in Q_{SW} and Q_{LH} carry over considerably in the Q_{net} biases estimated from ERA-I,
334 JRA-55 and MERRA-2. Thus the blended product, TropFlux, captures the observed Q_{net} with
335 greater skill than the reanalysis products.

336 Similar results are found between the reanalysis products and in situ data at other BoB RAMA
337 buoy locations: 90°E , 12°N (b27; Fig. S1) and 90°E , 8°N (b26; Fig. S2). Based on the 4 metrics
338 presented here, SST and V perform consistently well at all 3 locations; T_a struggles showing lower
339 correlations and poorer skill scores at b27 and b26 (more so than at b28) and as a result ΔT and
340 Q_{SH} are similarly poorly represented across most products. For Q_{LH} , results are consistently poor
341 and only TropFlux shows a skill score greater than zero. Last, Q_{SW} performs similarly between
342 products for all 3 buoys, i.e. ERA-I and TropFlux are able to reasonable reproduce Q_{SW} while
343 remaining products perform poorly based on mean differences, correlations, variance ratio and
344 skill score.

345 Based on the four metrics presented here, we find that ERA-I captures radiative fluxes best while
346 TropFlux is better at capturing the turbulent and net heat fluxes. In general, however, Q_{SW} and Q_{LH}
347 (and Q_{net} by association) are the variables that are the hardest to capture across all products. This
348 is evident in the low correlations, large biases and low skill scores. Since errors in Q_{net} can cause
349 large errors in SST in the BoB and affect the accurate representation of monsoon processes from
350 reanalysis products, the next section investigates the flux components in more depth.

351 **4. Surface Fluxes at RAMA flux reference site b28**

352 SST variability in the BoB is mainly driven by surface heat fluxes (Sengupta and Ravichandan
353 2001). Accurate representation of meteorological variables and the associated fluxes in reanalysis

354 products is therefore crucial for the correct representation of monsoon related variability. The
355 individual components of surface heat fluxes are further investigated here.

356 Fig. 3 shows scatterplots of the Q_{net} vs each flux component from RAMA b28, ERA-I, TropFlux,
357 JRA-55, MERRA-2 and CFSR. Individual daily means are plotted as points and contour lines en-
358 close 10% and 50% of points in the each joint distribution (calculated with R function HPDre-
359 gionplot in the emdbook package, Bolker (2008)). Fig. 3a shows the relationship between Q_{SW}
360 and Q_{net} at b28. Q_{SW} is the main driver of Q_{net} with a strong positive correlation ($r=0.93$). Q_{LW}
361 is anticorrelated with Q_{net} ($r=-0.58$, Fig. 3b) as increased cloud cover reduces the heat gain by the
362 ocean by Q_{SW} and reduces the heat loss by the ocean by Q_{LW} . Both Q_{LH} and Q_{SH} are positively
363 correlated with Q_{net} ($r=0.68, 0.63$ respectively, Fig. 3c,d) but Q_{LH} is an order of magnitude larger.

364 ERA-I shows similar correlations to b28, the correlations for the radiative components (Q_{SW}
365 and Q_{LW}) being slightly less correlated with Q_{net} than for B28 and the turbulent components (Q_{LH}
366 and Q_{SH}) more correlated. The underestimate of variability in Q_{SW} and Q_{LW} by ERA-I is clear
367 in Figs. 3e, f, and the overestimate of Q_{LH} and resulting bias in Q_{net} in Fig. 3g. The adjustments
368 applied to ERA-I to give TropFlux perform well for the turbulent fluxes (Figs. 3k, l) given better
369 alignment of the distributions in addition to reducing biases. However the radiative estimates from
370 TropFlux are worse than ERA-I. TropFlux Q_{SW} is constructed from ISCCP, until 2007, and bias
371 corrected ISCCP mean seasonal cycle and NOAA OLR to present; hence, TropFlux Q_{SW} biases are
372 likely linked to the algorithm used in KP12. TropFlux Q_{SW} shows improved (higher) variability,
373 but shifts the peak of the distribution to even lower values than ERA-I (compare Figs. 3e, i). The
374 adjustments applied to ERA-I Q_{LW} to give TropFlux give worse performance compared with b28
375 (Figs. 3f, j).

376 The remaining 3 products (JRA-55, MERRA-2 and CRSR, Figs. 3m-x) all show poor agreement
377 with the relationships between the flux components and Q_{net} , as expected from the skill scores

378 presented in Fig. 2. The exception is the good agreement shown for CFSR Q_{SH} (Fig. 3x) but only
379 due to the compensating biases in CFSR Q_{net} .

380 De-constructing turbulent fluxes into their meteorological components provides further insight
381 into differences among products, and helps determine if errors and biases in Q_{SH} (Q_{LH}) at the
382 buoy location (Fig. 2a) originate from errors in the wind field or air-sea contrasts in temperature
383 (humidity). Fig. 4a-f shows scatterplots of Q_{LH} vs the individual components of Q_{LH} : Δq and V .
384 The largest contributing factor to Q_{LH} variability across all products is V , where increases in V are
385 linked with increases in Q_{LH} (Fig. 4d). The correlation between Δq and Q_{LH} is lower (Fig. 4a) as
386 Δq and V are anti-correlated (Fig. 4g). This anti-correlation is well-captured by ERA-I (Fig. 4h)
387 with a slight overestimate of Δq . The TropFlux corrections result in a underestimation of Δq , but
388 despite this the Q_{LH} agrees reasonably with b28, perhaps due to the gustiness adjustment to wind
389 in the flux calculation.

390 ΔT is the strongest control on Q_{SH} (Fig. 4j) with V contributing little to the variability (Fig. 4m)
391 of Q_{SH} . This is consistent with the finding that Q_{SH} variability is particularly sensitive to SST
392 fluctuations (compared to Q_{LH}) in the tropical Indian Ocean at intraseasonal time scales (DeMott
393 et al. 2014). Both ERA-I (Fig. 4k) and TropFlux (Fig. 4l) overestimate the variability in ΔT . ERA-
394 I is biased toward unstable atmospheric conditions (ΔT positive) and TropFlux over-represents
395 stable conditions. The TropFlux Q_{SH} is strongly skewed compared to b28, but the representation of
396 Q_{SH} is overall better than ERA-I (Fig. 2d). The relationship between the radiative flux components
397 at b28 (Fig. 4s) is better captured by ERA-I (Fig. 4t) than TropFlux (Fig. 4u).

398 In general, Q_{net} is largely driven by Q_{SW} and Q_{LH} ; Q_{LH} variability is driven by V and (to a lesser
399 extent) Δq , and Q_{SH} variability is mostly driven by ΔT . Results here suggest errors/biases in Q_{LH}
400 originate from both the wind field and the Δq and, as Q_{SH} shows negligible dependence on V , the

401 biases from the observed Q_{SH} are more likely to be linked with errors in the ΔT . Q_{SW} and Q_{LH} are
402 the variables the reanalysis and blended products have the most difficulty reproducing (Section 3).

403 **5. Air-Sea fluxes across the Bay of Bengal**

404 *a. Mean fields*

405 In this section, air-sea fluxes at all points in the BoB from the reanalysis products are compared
406 to determine how much of the variability observed at the RAMA buoy sites is localized.

407 Figure 5 shows turbulent fluxes from five data products averaged over the summer (JJAS) mon-
408 soon season, from 2007 to 2015, across the BoB. The Q_{SH} values from JRA-55 and (to a lesser
409 extent) ERA-I show higher negative (upward) flux values, indicating greater heat loss from ocean
410 to atmosphere, than the other 3 products. This is consistent with biases seen in section 3 (Fig. 2a),
411 where JRA-55 and ERA-I overestimated the observed Q_{SH} . Differences in spatial gradients be-
412 tween products occur near b28 (black square, Fig. 5), where TropFlux, ERA-I and CFSR show
413 a larger gradient decreasing from east to west across the buoy, and MERRA-2 and JRA-55 show
414 almost no gradient. Other spatial differences are apparent in the patterns across coastal waters of
415 the BoB, such as the region around Sri Lanka and the east coast of India, where only TropFlux
416 and CFSR show regions of positive Q_{SH} (i.e. heat gain to the ocean). (We note the smaller con-
417 tour range in Q_{SH} values, -20 to 20 W m^{-2} compared with Q_{LH} , -200 to 0 W m^{-2}). For the
418 mean Q_{LH} field, all products show a region of strong Q_{LH} centred on the southern part of the
419 BoB, sandwiched between the equator and 10°N , covering the zonal extent of the basin. This pool
420 of elevated Q_{LH} in the southern BoB appears largest and strongest in JRA-55 and CFSR, and in
421 TropFlux the pool is shifted further south and is considerably weaker compared to the remaining
422 reanalysis products. Near b28 most products show a strong gradient in Q_{LH} decreasing from south

423 to north, though in JRA-55 this gradient is slightly more sloped in the southwest to northeast di-
424 rection. These patterns are consistent with the mean and standard deviation of the Q_{SH} and Q_{LH}
425 from all products (Fig. S3). Combining these results with the biases and skill scores from sec-
426 tion 3, where it was shown that Q_{LH} from TropFlux underestimates the observed Q_{LH} at b28 and
427 the reanalysis products all overestimate the observed Q_{LH} by a wide margin on the order of 50 to
428 75 W m^{-2} , suggests TropFlux captures turbulent fluxes best, and the erroneously enhanced Q_{LH}
429 seen at the b28 location in ERA-I, JRA-55, MERRA-2 and CFSR shows large-scale coherence
430 across the BoB.

431 In section 3, Q_{SW} was shown to have some of the largest biases in the reanalysis products when
432 compared with the in situ Q_{SW} from RAMA b28 data. It follows that in Fig. 6, the mean Q_{SW}
433 fields over the BoB show a wide range in Q_{SW} values (~ 100 to 250 W m^{-2}), differing quite
434 substantially between products: CFSR and MERRA-2 show higher and lower values, respectively,
435 of Q_{SW} when compared to ERA-I, TropFlux and JRA-55. The mean Q_{SW} field across the BoB
436 depicts regions of high Q_{SW} in the vicinity of Sri Lanka and southwest of the southernmost tip
437 of India, from the equator to 5°N in ERA-I, in TropFlux and JRA-55, but not in the MERRA-2
438 or CFSR products, consistent with dry slot in the rain shadow of Sri Lanka (Puvaneswaran and
439 Smithson 1991). Since the smallest biases (which are negative) were observed in JRA-55 and
440 ERA-I in section 3 (Fig. 2a), these results suggest TropFlux and (to a greater degree) MERRA-2
441 values are underestimating the observed Q_{SW} across the basin, while CFSR is overestimating them
442 across the basin on an order of 70 W m^{-2} . CFSR also shows the greatest departure from the spatial
443 patterns across the BoB than any of the other products, failing to capture the region of high Q_{SW}
444 around Sri Lanka and southeast India (Fig. S3). The difference in the range of Q_{LW} values across
445 products is considerably smaller, consistent with section 3, where it was shown that the Q_{LW} had
446 some of the smallest biases among the flux components (Fig. 2a). The mean field for Q_{LW} appears

447 to show a more consistent pattern in spatial gradients from all products across the BoB, compared
448 to Q_{SW} (Fig. 6; right hand column). In general, there is a high to low (south to north) gradient in
449 Q_{LW} across the BoB.

450 Q_{net} for ERA-I, JRA-55 and MERRA-2 depict large heat loss in the central and southern regions
451 of the BoB (Fig. S4), which is consistent with the results shown in section 3 (Fig. 2). TropFlux
452 and CFSR, on the other hand, depict a net heat gain by the ocean all across the basin and strongest
453 in the southwest and northern parts of the basin. In particular, values for Q_{net} in CFSR are the
454 product of errors in the Q_{LH} and Q_{SW} components cancelling out. Since the patterns of variability
455 are generally similar across the basin for all products (Fig. 6), results from section 3 wherein
456 TropFlux underestimates observed Q_{LW} and all remaining products overestimate the observed Q_{LW}
457 at RAMA b28 (Fig. 2a) are taken to be representative of the basin wide biases in the BoB.

458 *b. Monsoon Variability: The Boreal Summer Intraseasonal Oscillation*

459 In the previous sections, the performance of the reanalysis products in simulating the day-to-day
460 variability at a point location in the BoB (sections 3, 4) and the time-mean spatial patterns over
461 the BoB (section 5a) was assessed. Another necessary capability of a reanalysis product is that
462 it should be able to simulate the main spatial and temporal patterns of variability within a given
463 region, as these modes are the likely sources of potential predictability in a forecast system that
464 uses reanalysis products as a forcing input. The boreal summer intraseasonal oscillation (BSISO)
465 is one of the primary modes of variability associated with the Asian summer monsoon (Webster
466 et al. 1998; Lee et al. 2013). The BSISO is also known as the Monsoon Intraseasonal Oscillation
467 (MISO; Suhas et al. 2013), and was first identified as northward-propagating 30-60-day bands of
468 clouds and convection over India by, e.g., Sikka and Gadgil (1980). It is often recognised as the
469 northern summer counterpart to the Madden-Julian Oscillation (MJO; Madden and Julian, 1994).

470 Here the BSISO index from Lee et al. (2013) is used to assess the representation of boreal summer
471 intraseasonal variability from the reanalysis products.

472 Similar to the MJO (Wheeler and Hendon 2004), the BSISO indices are constructed from multi-
473 variate empirical orthogonal function analysis of satellite OLR and the 850-hPa zonal wind fields
474 from NCEP-DOE reanalysis in the region of the Asian summer monsoon (Lee et al. 2013). The
475 first two principal components (PC) of the BSISO form the BSISO1, which corresponds to the
476 northward propagating component of the summer monsoon and has a 30–60 day period (Wang
477 et al. 2005). The third and fourth PC of the BSISO form the BSISO2, which is the north-
478 ward/northwestward component of the monsoon, usually associated with the pre-monsoon and
479 monsoon onset periods, and has a period of 10-20 days (Kikuchi and Wang 2010). Here we focus
480 on the 30–60 day northward propagating BSISO, i.e. the BSISO1.

481 The BSISO1 mode is divided into eight phases, each phase covering one-eighth of the cycle
482 (Lee et al. 2013). During phase 1, a zonally elongated band of enhanced atmospheric convection
483 lies over the equatorial Indian Ocean, while a band of suppressed convection extends from India
484 southeastward across the BoB, southeast Asia and into the equatorial western Pacific (Fig. 7).
485 Over phases 2, 3 and 4, the band of enhanced convection moves northward and eastward, while
486 the suppressed convection retreats to the northeast and contracts. A second band of suppressed
487 convection then starts to develop over the equatorial Indian Ocean, such that the anomalies at
488 phase 5 are approximately the opposite sign to those at phase 1 (a half cycle earlier). The new
489 band of suppressed convection then propagates northeastward during phases 6, 7, and 8. Finally,
490 enhanced convection re-establishes itself over the equatorial Indian Ocean again in phase 1, and
491 the next cycle begins.

492 The BSISO1 composites here are constructed using an index of BSISO1 phases (1–8) based on
493 satellite OLR and 850hPa zonal wind fields as described in Lee et al. (2013) and made available

494 through the APEC Climate Centre data portal: <http://www.apcc21.net/ser/casts.do?lang=en>. For
495 each variable V , wind direction, Q_{SW} , Q_{LH} and Q_{net} , daily anomalies were computed from the
496 monthly mean for the monsoon season (JJAS) 2007 to 2015. Then, each day during the study
497 period was allocated to one of the eight BSISO1 phases, or was discarded if the overall BSISO1
498 amplitude was weak (i.e., $\sqrt{PC1^2 + PC2^2} < 1$). Data from each product were averaged over the
499 days in each phase to obtain the eight phase composites of the life cycle.

500 The BSISO1 representations in each reanalysis product are first validated against the *in situ*
501 data at the RAMA b28 location. Fig. 8 shows the median, interquartile range, 95% confidence
502 intervals and outliers for V , wind direction, Q_{SW} , Q_{LH} and Q_{net} from the in situ data and the ERA-
503 I, TropFlux and CFSR products at each phase of the BSISO1 life cycle. During phase 1 (2) all
504 products overestimate (underestimate) the observed BSISO1 V and, in general, all do a reasonable
505 job of capturing the observed V during BSISO1 phases 3 to 8 (Fig. 8a-d). The prevailing surface
506 winds remain approximately from the south west during JJAS, as measured by the buoy and in all
507 the products at the buoy location (Fig. 8e-h). The change in surface wind direction through the
508 cycle is less well represented in the products. During phases 1 through 3, the buoy shows winds
509 becoming more southerly, whereas all of the products show a change to more westerly winds
510 during these phases.

511 The RAMA Q_{SW} measurements show high median values in phases 1 to 3 (Fig. 8i), during the
512 convectively suppressed part of the BSISO1 cycle in the northern BoB (Fig. 7). As the enhanced
513 convection moves into the BoB, cloud cover increases and the Q_{SW} values decrease during phases
514 4, 5 and 7. Although the reanalysis products do reproduce this qualitative pattern, they all under-
515 estimate the amplitude of the Q_{SW} variability associated with the BSISO1 (Fig. 8j-l). In particular,
516 ERA-I and TropFlux tend to underestimate (overestimate) highs (lows) in the observed Q_{SW} within
517 a range of $\pm 45 \text{ W m}^{-2}$; meanwhile though CFSR also generally underestimates the amplitude of

518 the variability, it grossly overestimates Q_{SW} values (associated with BSISO1) in comparison with
519 the observed Q_{SW} , with up to values of 75 W m^{-2} . These results are consistent with section 3,
520 where it was shown that ERA-I and (to a lesser degree) TropFlux reasonably estimated the ob-
521 served Q_{SW} , based on skill score; and, CFSR showed large positive biases, low correlation and
522 poor skill score for Q_{SW} . Hence, in an ocean model forced by one of these products, the heating
523 of the ocean surface by Q_{SW} during the suppressed convective phase, and the cooling during the
524 active convective phase of the BSISO1 would both be severely misrepresented.

525 The systematic error apparent in Q_{SW} is compensated to a certain degree by a systematic error in
526 Q_{LH} of similar magnitude (Fig. 8n-p). The Q_{LH} at the RAMA b28 location shows low median Q_{LH}
527 values in phases 1 to 3, indicating reduced cooling of the ocean surface, and higher Q_{LH} values
528 from phases 5 to 7, indicating increased cooling of the ocean surface (Fig. 8m). The TropFlux
529 product does best at capturing the Q_{LH} BSISO1 variability and magnitude. The other data products
530 appear to generally capture the observed variability correctly; however, both ERA-I and (to a
531 greater extent) CFSR largely overestimate the median values of the observed Q_{LH} , indicating
532 erroneously high cooling of the ocean surface. The significantly reduced bias in NHF from CFSR
533 throughout all phases (Fig. 8t) indicates the systemic error in Q_{SW} is being largely compensated for
534 by the systemic error in Q_{LH} . Hence, in the case of CFSR and (to much smaller extent) TropFlux,
535 the erroneous strong cooling of the ocean surface from high Q_{LH} values offsets the erroneous high
536 heating of the ocean surface from the Q_{SW} values. ERA-I generally captures the observed BSISO1
537 Q_{net} variability; however, the Q_{SW} and Q_{LH} offsets add up and yield a Q_{net} of a sign opposite to
538 the observed, consistent with Fig. 2.

539 ERA-I has a similar pattern of Q_{SW} and Q_{LH} biases, but the magnitude of errors is smaller in
540 comparison to CFSR. The blended product, TropFlux, shows similar offsets in the Q_{SW} ; however,
541 its Q_{LH} and Q_{net} is more realistic and appears to capture best the observed BSISO1 Q_{SW} and Q_{LH}

542 variability. These results are consistent with section 3, where it was showed that in general ERA-I
543 does better at capturing radiative fluxes and TropFlux captures turbulent and net heat fluxes best.
544 To calculate Q_{SW} , TropFlux uses observed cloudiness data from ISCCP up until 2009 (when it was
545 last available), and the ISCCP mean seasonal cycle and NOAA OLR thereafter (KP12); while the
546 four reanalysis products use their internally generated cloud fields, which are dependent on their
547 convective and microphysical parameterization schemes. This highlights the well-known major
548 errors in these schemes (e.g. Boilley and Wald 2015). These errors clearly impact intraseasonal
549 variability as well as the mean fields.

550 Fig. 9 shows composites of daily anomalies from the monthly mean for the summer season
551 (JJAS) from 2007 to 2015 for Q_{SW} , Q_{LH} , V and q_a during the most extreme phases, 2 and 5, of the
552 BSISO1 life cycle over the BoB from TropFlux (shaded) and ERA-I (contour lines). During phase
553 2, both products depict large positive Q_{SW} anomalies in the northern BoB, and negative Q_{LH} and
554 V anomalies in the eastern BoB (Fig. 9 a, b, c), indicating clear skies and suppressed convection
555 in that region. In phase 5, the anomalies have flipped sign, and there is an elongated zonal band of
556 negative Q_{SW} anomalies, and positive Q_{LH} and V anomalies across the BoB, indicating enhanced
557 convection, in agreement with the BSISO1 life cycle from NOAA OLR and NCEP wind fields
558 (Fig. 7) and the BSISO1 life cycle at the RAMA b28 location (Fig. 8). Generally, both TropFlux
559 and ERA-I consistently capture the correct patterns of variability associated with the BSISO1 at
560 phase 2 and 5 (see Fig. 7). However, ERA-I shows weaker Q_{SW} anomalies and stronger Q_{LH}
561 anomalies than TropFlux, consistent with results observed at the RAMA b28 location that suggest
562 TropFlux is more accurate at this location (Fig. 8).

563 In contrast, the BSISO1 life cycles of Q_{SW} and Q_{LH} in JRA-55, MERRA-2 and CFSR are shown
564 to be noisier (Fig. 10) than their counterparts in TropFlux and ERA-I, especially during phase 5.
565 During phase 5, usually characterized by a zonal band of enhanced convection in the northern

566 BoB, JRA-55 only captures a weakened band of negative Q_{SW} anomalies in the northernmost and
567 easternmost parts of the BoB (Fig. 10d). In MERRA-2, the BSISO1 signal is barely perceptible
568 from the Q_{SW} , and in CFSR the band of Q_{SW} variability is weakened and shifted south (Fig. 10e,
569 f). CFSR further shows exaggeratedly high positive Q_{LH} anomalies that compensate for the Q_{SW}
570 bias. The diminished Q_{SW} variability in MERRA-2 can likely be attributed to the MERRA-2
571 negative bias, low correlation and poor skill score in Q_{SW} (Fig. 2). The difficulties of MERRA-
572 2, JRA-55 and CFSR in capturing the BSISO1 signal across the basin is consistent with their
573 difficulties capturing the BSISO1 variability at RAMA b28 (Fig. 8) and can be directly attributed
574 to the products difficulties in representing surface fluxes, as seen in the previous sections (i.e.
575 section 3, 4). In general, TropFlux and ERA-I captured the observed BSISO1 Q_{SW} best, and
576 TropFlux captured the observed BSISO1 Q_{LH} and Q_{net} best; both products depicted a life cycle
577 composite which was encouragingly similar to the Lee et al. (2013) OLR life cycle (Fig. 8).

578 Finally, we note that with low wind speeds and high radiation, the effectiveness of the radiation
579 shields on the T_a and humidity sensor decreases (Anderson and Baumgartner 1998). Anderson
580 and Baumgartner (1998) estimated that for naturally ventilated sensors, errors of up to 3.4°C in
581 the mean daytime temperature could lead to biases of 22 W m^{-2} in the turbulent fluxes. Here
582 the T_a and humidity sensor aboard the ATLAS moorings used multi-plate radiation shield and
583 are naturally ventilated, hence high radiation and low wind speeds may result in less effective
584 radiation shields (Freitag et al. 2001). Specifically, manufacturer estimates that for radiation above
585 1080 W m^{-2} and winds at or below 3 m s^{-1} , the temperature bias can increase from 0.2°C to 0.4°C
586 (Freitag et al. 2001). During phase 1 of the BSISO1, when wind speeds drop to 3 m s^{-1} and the
587 solar radiation is quite high due to suppressed convection, there are greater chances of T_a errors
588 occurring due to failing radiation shields. However, careful examination of the T_a anomalies per
589 phase (not shown here) suggests there are no significant T_a errors. The high wind speed during the

590 majority of the phases (2 through 8) decreases the chances of radiation shields contributing to the
591 overall error.

592 **6. Summary and Conclusions**

593 In this study, five data products are analysed and compared with in situ data from a moored array
594 in the BoB to determine how well the reanalysis products characterise air-sea fluxes and intrasea-
595 sonal variability during the SW monsoon season. Specifically, meteorological parameters, SST ,
596 V , T_a and q_a , air-sea temperature difference, ΔT , air-sea humidity difference, Δq , and fluxes, Q_{SW} ,
597 Q_{LW} , Q_{SH} , Q_{LH} and Q_{net} from ERA-I, TropFlux, JRA-55, MERRA-2 and CFSR were evaluated
598 for JJAS from 2007–2015, and compared with in situ data from the RAMA surface flux reference
599 site at 15°N , 90°E , denoted b28. In general, most products did reasonably well at representing
600 the meteorological variables, though q_a had the lowest correlations, highest biases and lowest skill
601 scores across all products (Fig. 2). TropFlux and ERA-I performed best, while the coupled prod-
602 uct, CFSR, exhibited some of the largest biases. From the flux variables, Q_{SW} and Q_{LH} were
603 shown to be the main drivers of the observed Q_{net} variability, but were also the two variables the
604 products had the most difficulty capturing. Correlations were lowest for the radiative fluxes and
605 Q_{SH} , and there were non-negligible biases in the range of 50 W m^{-2} in Q_{SW} . For Q_{LH} , all products
606 other than TropFlux overestimated the observed Q_{LH} by at least 40 W m^{-2} , while the TropFlux
607 bias was $\sim 10 \text{ W m}^{-2}$. In general, based on mean biases, correlations and skill scores, ERA-I was
608 shown to capture radiative fluxes best, while TropFlux better captured turbulent and latent heat
609 fluxes. Skill scores indicated poor performance for Q_{LH} and the radiative fluxes in MERRA-2 and
610 CFSR, and we note that for the coupled ocean-atmosphere product CFSR, these biases canceled
611 each other out in the Q_{net} .

612 The temporal mean fields for the fluxes across the BoB were investigated in section 5a, where
613 various discrepancies were observed in the spatial patterns among the products. For Q_{SH} , the
614 patterns were consistent across ERA-I, TropFlux and CFSR, though JRA-55 and ERA-I had large
615 negative biases, indicating erroneously high heat loss to the atmosphere and therefore erroneous
616 cooling of the sea surface. Patterns of Q_{LH} variability were generally consistent across all products
617 (i.e. a region of high Q_{LH} in the southwest corner of the BoB), though values ranged on the order
618 of 40 W m^{-2} between the reanalysis products. For Q_{SW} , ERA-I outperformed the other three
619 products by a wide margin (CFSR, in particular, showed much higher values and different spatial
620 gradients than the other products). Differences in Q_{LH} and Q_{SW} in the reanalysis products were
621 generally attributed to differences or issues with the internally-generated cloud fields/schemes (e.g.
622 Wang et al. 2011; Boilley and Wald 2015). For Q_{LW} , though spatial gradients were consistent,
623 correlations high and biases small, skill scores were low (except for ERA-I) across all products. In
624 general, results from the temporal mean field indicate results at the b28 location are not localized,
625 and biases of similar magnitude to those seen at b28 will be widespread across the BoB. Further,
626 the biases in the fluxes implied by the meteorological parameters at b28 are likely representative of
627 the magnitude of biases observed in other regions in the basin, in the temporally-averaged fields.

628 The BSISO1 index, representative of the northward propagating component of the summer mon-
629 soon (with a 30–60 day periodicity), was used to test the ability of the different products to rep-
630 resent the principal mode of atmospheric variability in the BoB in this season, in particular in
631 the representation of Q_{SW} and Q_{LH} in ERA-I, TropFlux, and CFSR. Comparison with RAMA
632 b28 suggested TropFlux and ERA-I most reliably captured surface flux variability compared with
633 the observed BSISO1 Q_{SW} cycle at 15°N , 90°E ; however, TropFlux captured the variability and
634 magnitude of the observed Q_{LH} and Q_{net} best. The analysis of the mean fields, the comparison
635 with BSISO1 at b28, and comparison with Lee et al. (2013) satellite OLR maps allows us to ex-

636 tend this confidence over the entire BoB. Thus, both TropFlux and ERA-I appear to best represent
637 the variability of the surface fluxes at RAMA b28 and across the entire BoB basin. Conversely,
638 MERRA-2, CFSR and JRA-55 struggled to capture the climatic variability associated with the
639 BSISO1, with weak Q_{SW} variability at the location of RAMA b28 suggesting that the convective
640 signal is poorly represented in these products, while the over-estimation of Q_{LH} variability sug-
641 gests erroneous surface wind and humidity fields. Hence, we infer inability to accurately capture
642 or reproduce the surface fluxes at b28 or at mean field levels shows that the MERRA-2, CFSR and
643 JRA-55 products will similarly struggle to capture variability associated with the boreal summer
644 monsoon.

645 As air-sea fluxes have been shown to be key players in monsoon variability (Vecchi and Har-
646 rison 2002), caution is advised when selecting a data product to represent monsoonal processes.
647 This study has highlighted significant and critical deficiencies in reanalysis flux products from
648 the accumulated errors observed in the meteorological parameters and surface fluxes specific to
649 the southwest monsoon time period and have yet to be verified for the entire seasonal cycle. In
650 general, ERA-I and TropFlux were shown to outperform MERRA-2, JRA-55 and CFSR; ERA-
651 I represented radiative fluxes best, while TropFlux better captured turbulent and net heat fluxes.
652 Based on findings shown here, this analysis recommends TropFlux and ERA-I as the best available
653 products for the study of air-sea fluxes and intraseasonal variability over the BoB during the SW
654 monsoon, or for the forcing of ocean models during boreal summer in the tropical Indian Ocean.

655 *Acknowledgments.* The NERC BoBBLE project supported ASF and ECK (NE/L013835/1),
656 BGMW (NE/L013827/1), and SCP (NE/L013800/1). PNV thanks the Ministry of Earth
657 Sciences, Govt. of India for funding under the BoBBLE project. The authors thank
658 the US National Oceanic and Atmospheric Administration (NOAA)/Pacific Marine Environ-

659 mental Laboratory (PMEL) and National Institute of Oceanography (NIO) for access to
660 RAMA buoy data (<https://www.pmel.noaa.gov/tao/drupal/disdcl/>). The authors would also
661 like to acknowledge the European Centre for Medium Range Weather Forecasting for ERA-
662 Interim data access (<http://apps.ecmwf.int/datasets/data/interim-full-daily/levtype=pl/>); the Com-
663 putational and Information Systems Laboratory Research Data Archive (<https://rda.ucar.edu>)
664 for access to the reanalysis datasets JRA-55 and CFSR; the Global Modeling and As-
665 simulation Office (GMAO) and the GES DISC for the dissemination of MERRA-2
666 (<https://disc.sci.gsfc.nasa.gov/daac-bin/FTPSubset2.pl>); and, ESSO-INCOIS for TropFlux data
667 access (<http://www.incois.gov.in/tropflux/>). The TropFlux data is produced under a collab-
668 oration between Laboratoire d’Oceanographie: Experimentation et Approches Numeriques
669 (L’OCEAN) from Institut Pierre Simon Laplace (IPSL, Paris, France) and National Insti-
670 tute of Oceanography/CSIR (NIO, Goa, India), and supported by Institut de Recherche pour
671 le Developpement (IRD, France). TropFlux relies on data provided by the ECMWF Re-
672 Analysis interim (ERA-I) and ISCCP projects. The interpolated OLR and NCEP Reanalysis
673 data were provided by the NOAA/OAR/ESRL PSD, Boulder, Colorado, USA, from their web
674 site at <http://www.cdc.noaa.gov/>. The BSISO data were provided by the Apec Climate Cen-
675 tre through their website: <http://www.apcc21.net/ser/moni.do?lang=en>. The authors are grate-
676 ful to Dr. Shoji Hirahara of JMA for the JRA-55 daily SST data. The matlab version of
677 the COARE3.0 algorithm was used to estimate the uncertainty in the RAMA turbulent fluxes:
678 ftp://ftp.etl.noaa.gov/BLO/Air-Sea/bulkalg/cor3_0/. The authors are also grateful for the helpful
679 insight and comments from three anonymous reviewers.

680 **References**

- 681 Anderson, S. P., and M. F. Baumgartner, 1998: Radiative Heating Errors in Naturally Ventilated
682 Air Temperature Measurements Made from Buoys. *Journal of Atmospheric and Oceanic Tech-*
683 *nology*, **15** (1), 157–173.
- 684 Berrisford, P., P. Kållberg, S. Kobayashi, D. Dee, S. Uppala, A. J. Simmons, P. Poli, and H. Sato,
685 2011: Atmospheric conservation properties in ERA-Interim. *Quarterly Journal of the Royal*
686 *Meteorological Society*, **137** (659), 1381–1399, doi:10.1002/qj.864.
- 687 Boilley, A., and L. Wald, 2015: Comparison between meteorological re-analyses from ERA-
688 Interim and MERRA and measurements of daily solar irradiation at surface. *Renewable Energy*,
689 **75**, 135–143, doi:10.1016/j.renene.2014.09.042.
- 690 Bolker, B. M., 2008: *Ecological models and data in R*. Princeton University Press, 508 pp.
- 691 Bolton, D., 1980: The computation of equivalent potential temperature. *Monthly weather review*,
692 **108** (7), 1046–1053, doi:10.1175/1520-0493(1980)108<1046:TCOEPT>2.0.CO;2.
- 693 Bosilovich, M. G., and Coauthors, 2015: MERRA-2: Initial Evaluation of the Climate. *Series on*
694 *Global Modeling and Data Assimilation, NASA/TM*, **43** (104606), 1–139.
- 695 Brunke, M. A., Z. Wang, X. Zeng, M. Bosilovich, and C. Shie, 2011: An assessment of the
696 uncertainties in ocean surface turbulent fluxes in 11 reanalysis, satellite-derived, and combined
697 global datasets. *Journal of Climate*, **24** (21), 5469–5493.
- 698 Cronin, M. F., C. W. Fairall, and M. J. McPhaden, 2006: An assessment of buoy-derived and
699 numerical weather prediction surface heat fluxes in the tropical Pacific. *Journal of Geophysical*
700 *Research: Oceans*, **111** (C6), doi:10.1029/2005JC003324.

701 Dee, D. P., and S. Uppala, 2009: Variational bias correction of satellite radiance data in the ERA-
702 Interim reanalysis. *Quarterly Journal of the Royal Meteorological Society*, **135 (644)**, 1830–
703 1841, doi:10.1002/qj.493.

704 Dee, D. P., and Coauthors, 2011: The ERA-Interim reanalysis: Configuration and performance of
705 the data assimilation system. *Quarterly Journal of the Royal Meteorological Society*, **137 (656)**,
706 553–597, doi:10.1002/qj.828.

707 DeMott, C. A., C. Stan, D. A. Randall, and M. D. Branson, 2014: Intraseasonal Variability in Cou-
708 pled GCMs: The Roles of Ocean Feedbacks and Model Physics. *Journal of Climate*, **27 (13)**,
709 4970–4995, doi:10.1175/JCLI-D-13-00760.1.

710 Donlon, C. J., M. Martin, J. Stark, J. Roberts-Jones, E. Fiedler, and W. Wimmer, 2012: The
711 Operational Sea Surface Temperature and Sea Ice Analysis (OSTIA) system. *Remote Sensing*
712 *of Environment*, **116**, 140–158, doi:10.1016/j.rse.2010.10.017.

713 Duncan, B., and W. Han, 2009: Indian Ocean intraseasonal sea surface temperature variability
714 during boreal summer: Madden-Julian Oscillation versus submonthly forcing and processes.
715 *Journal of Geophysical Research: Oceans*, **114 (5)**, doi:10.1029/2008JC004958.

716 Fairall, C. W., E. F. Bradley, J. E. Hare, A. A. Grachev, and J. B. Edson, 2003: Bulk parameteriza-
717 tion of air-sea fluxes: Updates and verification for the COARE algorithm. *Journal of Climate*,
718 **16 (4)**, 571–591, doi:10.1175/1520-0442(2003)016<0571:BPOASF>2.0.CO;2.

719 Freitag, H. P., M. OHaleck, G. Thomas, and M. McPhaden, 2001: Calibration procedures and
720 instrumental accuracies for ATLAS wind measurements. *NOAA Tech. Memo. OAR PMEL*, **119**,
721 20.

- 722 Girishkumar, M. S., J. Joseph, V. P. Thangaprakash, V. Pottapinjara, and M. J. McPhaden, 2017:
723 Mixed Layer Temperature Budget for the Northward Propagating Summer Monsoon Intrasea-
724 sonal Oscillation (MISO) in the Central Bay of Bengal. *Journal of Geophysical Research:*
725 *Oceans*, **122** (11), 8841–8854.
- 726 Goswami, B. B., M. Deshpande, P. Mukhopadhyay, S. K. Saha, S. A. Rao, R. Murthugudde,
727 and B. N. Goswami, 2014: Simulation of monsoon intraseasonal variability in NCEP CFSv2
728 and its role on systematic bias. *Climate Dynamics*, **43** (9-10), 2725–2745, doi:10.1007/
729 s00382-014-2089-5.
- 730 Ishii, M., A. Shouji, S. Sugimoto, and T. Matsumoto, 2005: Objective analyses of sea-surface
731 temperature and marine meteorological variables for the 20th century using ICOADS and the
732 Kobe Collection. *International Journal of Climatology*, **25** (7), 865–879, doi:10.1002/joc.1169.
- 733 Kikuchi, K., and B. Wang, 2010: Formation of Tropical Cyclones in the Northern Indian Ocean
734 Associated with Two Types of Tropical Intraseasonal Oscillation Modes. *Journal of the Meteoro-*
735 *logical Society of Japan*, **88** (3), 475–496, doi:10.2151/jmsj.2010-313.
- 736 Kobayashi, S., and Coauthors, 2015: The JRA-55 Reanalysis: General Specifications and Basic
737 Characteristics. *Journal of the Meteorological Society of Japan. Ser. II*, **93** (1), 5–48, doi:10.
738 2151/jmsj.2015-001.
- 739 Kumar, B. P., J. Vialard, M. Lengaigne, and M. J. Mcphaden, 2012: TropFlux: Air-Sea Fluxes for
740 the Global Tropical Oceans Description and evaluation against observations. *Climate Dynam-*
741 *ics*, **38** (7), 1521–1543, doi:10.1007/s00382-011-1115-0.
- 742 Lau, W. K. M., D. E. Waliser, and B. N. Goswami, 2012: South Asian monsoon. *Intraseasonal*
743 *variability in the atmosphere-ocean climate system*, Springer Berlin Heidelberg, 21–72.

- 744 Lee, J. Y., B. Wang, M. C. Wheeler, X. Fu, D. E. Waliser, and I. S. Kang, 2013: Real-time
745 multivariate indices for the boreal summer intraseasonal oscillation over the Asian summer
746 monsoon region. *Climate Dynamics*, **40** (1-2), 493–509, doi:10.1007/s00382-012-1544-4.
- 747 McPhaden, M., 2010: The Global Tropical Moored Buoy Array. *Proceedings of OceanObs'09:
748 Sustained Ocean Observations and Information for Society*, **9** (1), 668–682, doi:10.5270/
749 OceanObs09.cwp.61.
- 750 McPhaden, M. J., and Coauthors, 2009: RAMA: The research moored array for African-Asian-
751 Australian monsoon analysis and prediction. *Bulletin of the American Meteorological Society*,
752 **90** (4), 459–480, doi:10.1175/2008BAMS2608.1.
- 753 Murphy, A. H., 1988: Skill Scores Based on the Mean Square Error and Their Relationships
754 to the Correlation Coefficient. *Monthly Weather Review*, **116** (12), 2417–2424, doi:10.1175/
755 1520-0493(1988)116<2417:SSBOTM>2.0.CO;2.
- 756 Onogi, K., and Coauthors, 2007: The JRA-25 reanalysis. *Journal of the Meteorological Society of
757 Japan. Ser. II*, **85** (3), 369–432, doi:10.2151/jmsj.85.369.
- 758 Parampil, S. R., A. Gera, M. Ravichandran, and D. Sengupta, 2010: Intraseasonal response of
759 mixed layer temperature and salinity in the Bay of Bengal to heat and freshwater flux. *Journal
760 of Geophysical Research: Oceans*, **115** (5), doi:10.1029/2009JC005790.
- 761 Puvaneswaran, K. M., and P. A. Smithson, 1991: Precipitation elevation relationships over Sri
762 Lanka. *Theoretical and Applied Climatology*, **43** (3), 113–122, doi:10.1007/BF00867468.
- 763 R Core Team, 2015: R: A Language and Environment for Statistical Computing. URL [http://www.
764 r-project.org/](http://www.r-project.org/), {ISBN} 3–900051–07–0 pp., doi:ISBN3-900051-07-0, /www.R-project.org.

765 Rienecker, M., and Coauthors, 2011: MERRA-NASA's Modern-Era Retrospective Analysis for
766 Research and Applications. *Bulletin of the American Meteorological Society*, **24 (14)**, 3624–
767 3648, doi:10.1175/JCLI-D-11-00015.1.

768 Saha, S., and Coauthors, 2010: The NCEP climate forecast system reanalysis. *Bulletin of*
769 *the American Meteorological Society*, **91 (8)**, 1015–1057, doi:10.1175/2010BAMS3001.1,
770 9809069v1.

771 Saha, S., and Coauthors, 2011: NCEP Climate Forecast System Version 2 (CFSv2) 6-hourly Prod-
772 ucts. URL <http://dx.doi.org/10.5065/D61C1TXF>, doi:10.5065/D61C1TXF.

773 Schiller, A., and J. Godfrey, 2003: Indian Ocean intraseasonal variability in an ocean general cir-
774 culation model. *Journal of Climate*, **16 (1999)**, 21–39, doi:10.1175/1520-0442(2003)016<0021:
775 IOIVIA>2.0.CO;2.

776 Sengupta, D., and M. Ravichandan, 2001: Oscillations of the Bay of Bengal SST during the 1998
777 summer monsoon. *Geophys. Res. Lett.*, **28 (10)**, 2033–2036, doi:10.1029/2000GL012548.

778 Sikka, D. R., and S. Gadgil, 1980: On the Maximum Cloud Zone and the ITCZ over Indian,
779 Longitudes during the Southwest Monsoon. *Monthly Weather Review*, **108 (11)**, 1840–1853,
780 doi:10.1175/1520-0493(1980)108<1840:OTMCZA>2.0.CO;2.

781 Suhas, E., J. M. Neena, and B. N. Goswami, 2013: An Indian monsoon intraseasonal oscillations
782 (MISO) index for real time monitoring and forecast verification. *Climate Dynamics*, **40 (11)**,
783 2605–2616, doi:10.1007/s00382-012-1462-5.

784 Vecchi, G. A., and D. E. Harrison, 2002: Monsoon breaks and subseasonal sea surface tem-
785 perature variability in the Bay of Bengal. *Journal of Climate*, **15 (12)**, 1485–1493, doi:
786 10.1175/1520-0442(2002)015<1485:MBASSS>2.0.CO;2.

- 787 Vialard, J., A. Jayakumar, C. Gnanaseelan, M. Lengaigne, D. Sengupta, and B. N. Goswami, 2011:
788 Processes of 3090 days sea surface temperature variability in the northern Indian Ocean during
789 boreal summer. *Climate Dynamics*, **38 (9-10)**, 1901–1916, doi:10.1007/s00382-011-1015-3.
- 790 Vinayachandran, P. N., V. S. N. Murty, and V. R. Babu, 2002: Observations of barrier layer forma-
791 tion in the Bay of Bengal during summer monsoon. *Journal of Geophysical Research: Oceans*,
792 **107 (C12)**, 2156–2202, doi:10.1029/2001JC000831.
- 793 Vinayachandran, P. N., and Coauthors, 2018: BoBBLE (Bay of Bengal Boundary Layer Experi-
794 ment): Ocean-atmosphere interaction and its impact on the South Asian monsoon. *Bulletin of*
795 *the American Meteorological Society*, doi:10.1175/BAMS-D-16-0230.1.
- 796 Waliser, D. E., 2006: Intraseasonal variability. *The Asian Monsoon*, Springer Berlin Heidelberg,
797 Berlin, 203–257, doi:10.1007/3-540-37722-0_5.
- 798 Wallcraft, A. J., A. B. Kara, C. N. Barron, E. J. Metzger, R. L. Pauley, and M. A. Bourassa,
799 2009: Comparisons of monthly mean 10 m wind speeds from satellites and NWP products
800 over the global ocean. *Journal of Geophysical Research Atmospheres*, **114 (16)**, doi:10.1029/
801 2008JD011696.
- 802 Wang, B., P. J. Webster, and H. Teng, 2005: Antecedents and self-induction of active-break south
803 Asian monsoon unraveled by satellites. *Geophysical Research Letters*, **32 (4)**, 1–4, doi:10.1029/
804 2004GL020996.
- 805 Wang, W., P. Xie, S. H. Yoo, Y. Xue, A. Kumar, and X. Wu, 2011: An assessment of the surface
806 climate in the NCEP climate forecast system reanalysis. *Climate Dynamics*, **37 (7-8)**, 1601–
807 1620, doi:10.1007/s00382-010-0935-7.

808 Webster, P. J., V. O. Magaña, T. N. Palmer, J. Shukla, R. A. Tomas, M. Yanai, and T. Yasunari,
809 1998: Monsoons: Processes, predictability, and the prospects for prediction. *Journal of Geo-*
810 *physical Research: Oceans*, **103 (C7)**, 14 451–14 510, doi:10.1029/97JC02719, 0402594v3.

811 Weller, R., and Coauthors, 2016: Air-Sea Interaction in the Bay of Bengal. *Oceanography*, **29 (2)**,
812 28–37, doi:10.5670/oceanog.2016.36.

813 Wheeler, M. C., and H. H. Hendon, 2004: An All-Season Real-Time Multivariate MJO Index:
814 Development of an Index for Monitoring and Prediction. *Monthly Weather Review*, **132 (8)**,
815 1917–1932, doi:10.1175/1520-0493(2004)132(1917:AARMMI)2.0.CO;2, arXiv:1011.1669v3.

816 Xue, Y., B. Huang, Z. Z. Hu, A. Kumar, C. Wen, D. Behringer, and S. Nadiga, 2011: An assess-
817 ment of oceanic variability in the NCEP climate forecast system reanalysis. *Climate Dynamics*,
818 **37 (11-12)**, 2511–2539, doi:10.1007/s00382-010-0954-4.

819 Yang, B., X. Fu, and B. Wang, 2008: Atmosphere-ocean conditions jointly guide convection of
820 the Boreal Summer Intraseasonal Oscillation: Satellite observations. *Journal of Geophysical*
821 *Research Atmospheres*, **113 (11)**, doi:10.1029/2007JD009276.

822 Yu, L., X. Jin, and R. A. Weller, 2007: Annual, Seasonal, and Interannual Variability of
823 AirSea Heat Fluxes in the Indian Ocean. *Journal of Climate*, **20 (13)**, 3190–3209, doi:
824 10.1175/JCLI4163.1.

825 Zhang, Y., W. B. Rossow, A. A. Lacis, V. Oinas, and M. I. Mishchenko, 2004: Calculation of
826 radiative fluxes from the surface to top of atmosphere based on ISCCP and other global data
827 sets: Refinements of the radiative transfer model and the input data. *Journal of Geophysical*
828 *Research D: Atmospheres*, **109 (19)**, doi:10.1029/2003JD004457.

829 **LIST OF TABLES**

830 **Table 1.** Summary of reanalysis, blended* and in situ products used in this study. 39

831 **Table 2.** Summary of documented (*SST*, *V*, *T_a*, and *q_a*) uncertainties (McPhaden et al.
832 2009) and calculated (ΔT , Δq , Q_{SH} , and Q_{LH}) uncertainties from the RAMA
833 buoy instruments. 40

TABLE 1. Summary of reanalysis, blended* and in situ products used in this study.

<i>Product</i>	<i>Input SST</i>	<i>Resolution</i>	<i>Period</i>	<i>Reference</i>	<i>Flux method</i>
ERA-Interim	See Dee et al. (2011)	-Sub-daily (3, 6-hourly) -0.75° X 0.75°	1979 to present	Dee et al. (2011)	Model
TropFlux*	Bias corrected ERA-I	-Daily -1.0° X 1.0°	1979 to present	Kumar et al. (2012)	COARE 3.0
JRA-55	COBE SST (Ishii et al. 2005)	-Sub-daily (3, 6-hourly) -0.56° X 0.56°	1979 to present	Kobayashi et al. (2015)	Model
MERRA-2	See Bosilovich et al. (2015)	-Sub-daily (1-hourly) -0.5° X 0.625°	1980 to present	Bosilovich et al. (2015)	Model
CFSR	See Saha et al. (2011)	-Sub-daily (6-hourly) -0.5° X 0.5°	1979 to 2011 CFSv2: 2011 to pres.	Saha et al. (2010) Saha et al. (2011)	Model
RAMA array	Observed	-Sub-daily (1-hourly fluxes; 2-min radiation data; 10-min surface meteorological data)	2007 to present	McPhaden et al. (2009)	COARE 3.0

834 TABLE 2. Summary of documented (SST , V , T_a , and q_a) uncertainties (McPhaden et al. 2009) and calculated
 835 (ΔT , Δq , Q_{SH} , and Q_{LH}) uncertainties from the RAMA buoy instruments.

<i>Measurement</i>	<i>Uncertainty</i>
SST	$\pm 0.02^\circ C$
V	$\pm 0.2 \text{ m s}^{-1}$
T_a	$\pm 0.2^\circ C$
q_a	$\pm 0.2 \text{ g kg}^{-1}$
ΔT	$\pm 0.2^\circ C$
Δq	$\pm 0.28 \text{ g kg}^{-1}$
Q_{SH}	$\pm 2.5 \text{ W m}^{-2}$
Q_{LH}	$\pm 7.3 \text{ W m}^{-2}$

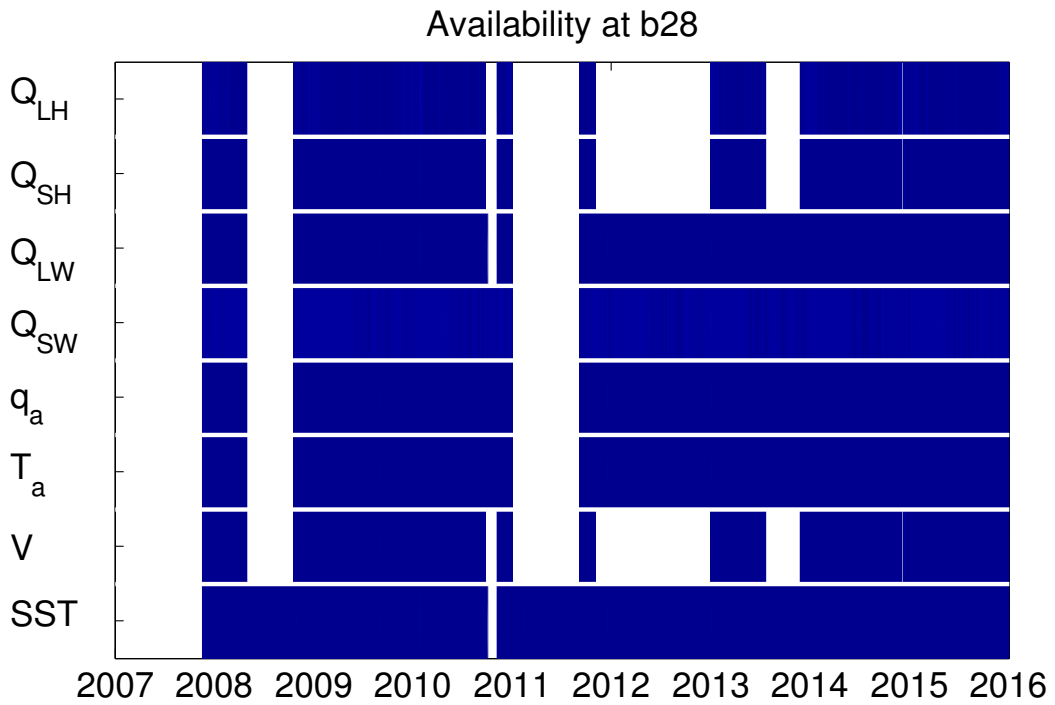
LIST OF FIGURES

836		
837	Fig. 1.	Availability of data at buoy site b28 (15°N and 90°E b28) for meteorological and flux parameters used in this study. 43
838		
839	Fig. 2.	Difference (product - RAMA; a), correlation (b), variance ratio (c), and skill score (d) for reanalysis products (ERA-I, TropFlux, JRA-55, MERRA-2 and CFSR) against data from RAMA b28. The 95% confidence intervals are shown in the difference, correlation and variance ratio metrics. The variables evaluated are the meteorological, SST (°C), V (m s^{-1}), T_a (°C), q_a (g kg^{-1}), ΔT (°C), Δq (g kg^{-1}), and flux, Q_{SW} (W m^{-2}), Q_{LW} (W m^{-2}), Q_{SH} (W m^{-2}), Q_{LH} (W m^{-2}), Q_{net} (W m^{-2}), for the summer (JJAS) from 2007 to 2015. Panel (a) shows uncertainties as per Table 2 indicated by the horizontal dashed lines, and a split scale to differentiate between meteorological and flux parameters. 44
840		
841		
842		
843		
844		
845		
846		
847	Fig. 3.	Scatterplots for Q_{net} vs each of Q_{SW} , Q_{LW} , Q_{SH} and Q_{LH} (all units in W m^{-2}) from RAMA buoy observations (a, b, c, d), ERA-I (e, f, g, h), TropFlux (i, j, k, l), JRA-55 (m, n, o, p), MERRA-2 (q, r, s, t) and CFSR (u, v, w, x) at site b28 (8°N and 90°E). Contour lines enclose the 10% and 50% of points in each joint distribution. RAMA contour lines (black) are repeated for comparison. 45
848		
849		
850		
851		
852	Fig. 4.	Scatterplots of Q_{LH} (W m^{-2}) vs Δq (g kg^{-1}), Q_{LH} (W m^{-2}) vs V (m s^{-1}), Δq (g kg^{-1}) vs V (m s^{-1}), Q_{SH} (W m^{-2}) vs ΔT (°C), Q_{SH} (W m^{-2}) vs V (m s^{-1}), ΔT (°C) vs V (m s^{-1}), and Q_{LW} (W m^{-2}) vs Q_{SW} (W m^{-2}) from RAMA buoy observations (left column), ERA-Interim (center column) and TropFlux (right column) at site b28 (8°N and 90°E). Contour lines enclose the 10% and 50% of points in each joint distribution. RAMA contour lines (black) are repeated for comparison. 46
853		
854		
855		
856		
857		
858	Fig. 5.	Mean Q_{SH} (left column; W m^{-2}) and Q_{LH} (right column; W m^{-2}) for ERA-I (a, f), TropFlux (b, g), JRA-55 (c, h), MERRA-2 (d, i), and CFSR (e, j). All fields are averaged for the SW monsoon season (JJAS) from 2007 to 2015. The black square indicates the location of the RAMA buoy, b28, in the Bay of Bengal. 47
859		
860		
861		
862	Fig. 6.	Same as in Fig. 5 but for radiative fluxes. 48
863	Fig. 7.	BSISO 1 life cycle composite of NOAA OLR anomalies (shaded; W m^{-2}) and NCEP-DOE 850-hPa wind anomalies (vector; m s^{-1}). 49
864		
865	Fig. 8.	Median, interquartile range, 95% confidence interval, and outliers for V (m s^{-1}), wind direction (°), Q_{SW} (W m^{-2}), Q_{LH} (W m^{-2}), and Q_{net} (W m^{-2}) vs BSISO1 phases (1 to 8) from RAMA b28 (a, e, i, m, q), ERA-I (b, f, j, n, r), TropFlux (c, g, k, o, s), and CFSR (d, h, l, p, t). The red line is the RAMA b28 median line, repeated for comparison. 50
866		
867		
868		
869	Fig. 9.	Composite of phase 2 (left column) and phase 5 (right column) of the BSISO1 life cycle. TropFlux (shaded) and ERA-I (contour lines) Q_{SW} anomalies at phase 2 (a) and phase 5 (e); Q_{LH} anomalies at phase 2 (b) and 5 (f); V anomalies at phase 2 (c) and 5 (g); and, q_a anomalies at phase 2 (d) and 5 (h). ERA-I Q_{SW} contour lines range from -40 to 40 W m^{-2} and Q_{LH} contour lines range from -30 to 30 W m^{-2} , with 5 W m^{-2} intervals. ERA-I V contour lines range from -3 to 3 m s^{-1} , with 0.5 m s^{-1} intervals. ERA-I q_a contour lines range from -1 to 1 g kg^{-1} , with 0.2 g kg^{-1} intervals. The black square indicates the location of the RAMA buoy 28. 51
870		
871		
872		
873		
874		
875		
876		
877	Fig. 10.	Phase 2 (left column) and 5 (right column) of the Q_{SW} (shading) and Q_{LH} (contour line) anomalies from JRA-55 (a, d), MERRA-2 (b, e), and CFSR (c, f) based on the BSISO1
878		

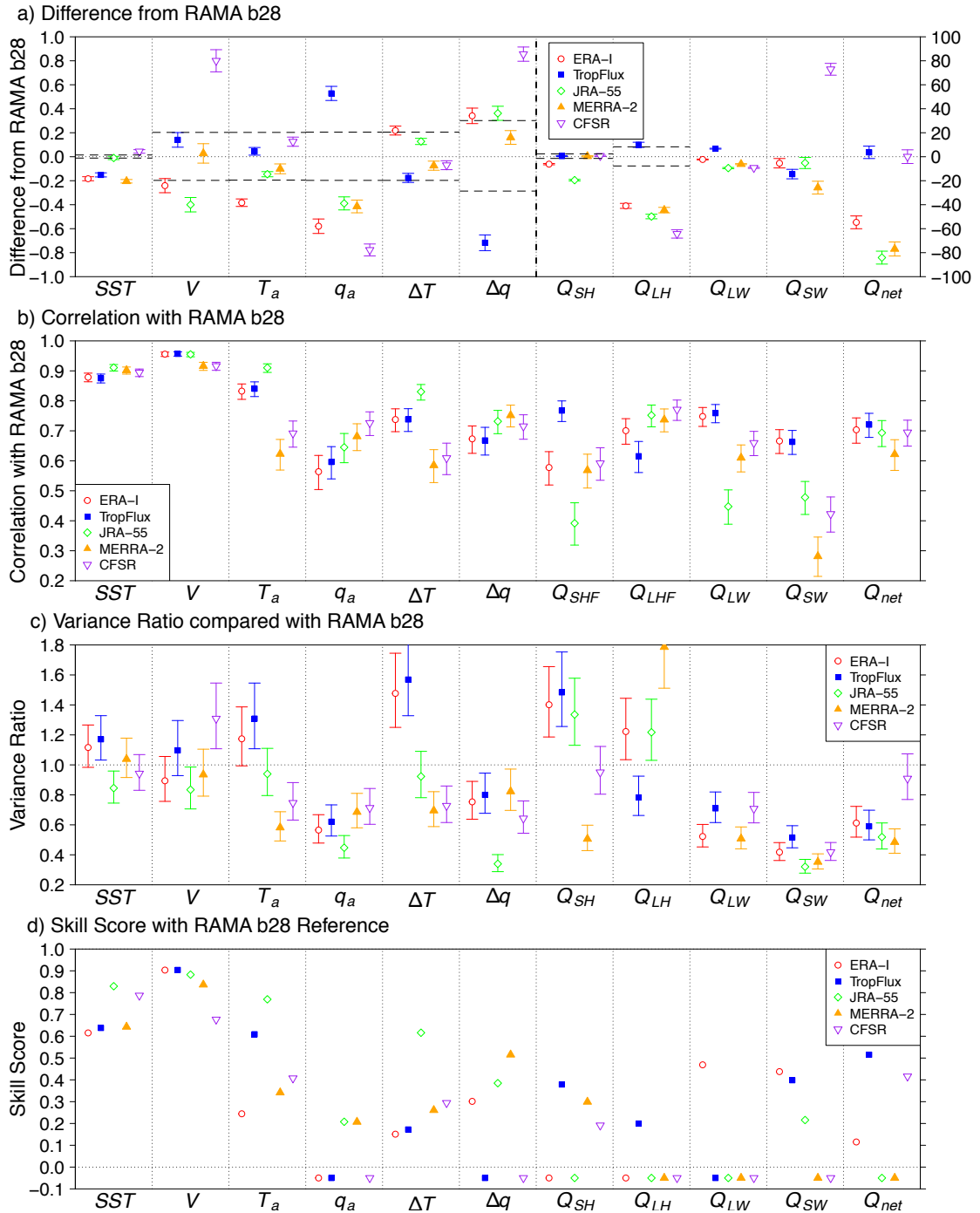
879

880

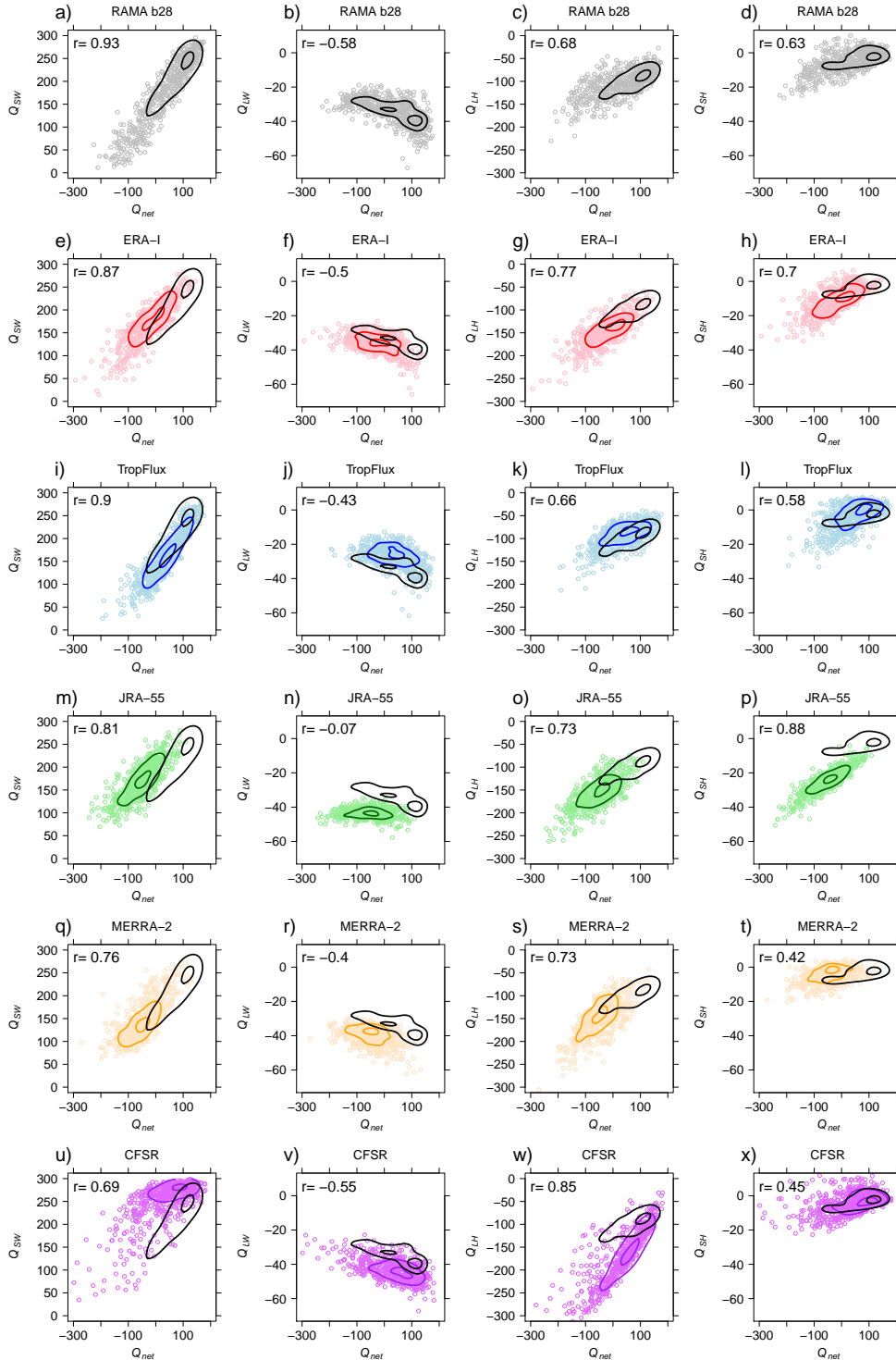
phases. Q_{LH} contour lines range from -40 to 40 $W m^{-2}$, with 5 $W m^{-2}$ intervals. The black square indicates the location of the RAMA buoy 28. All units in $W m^{-2}$ 52



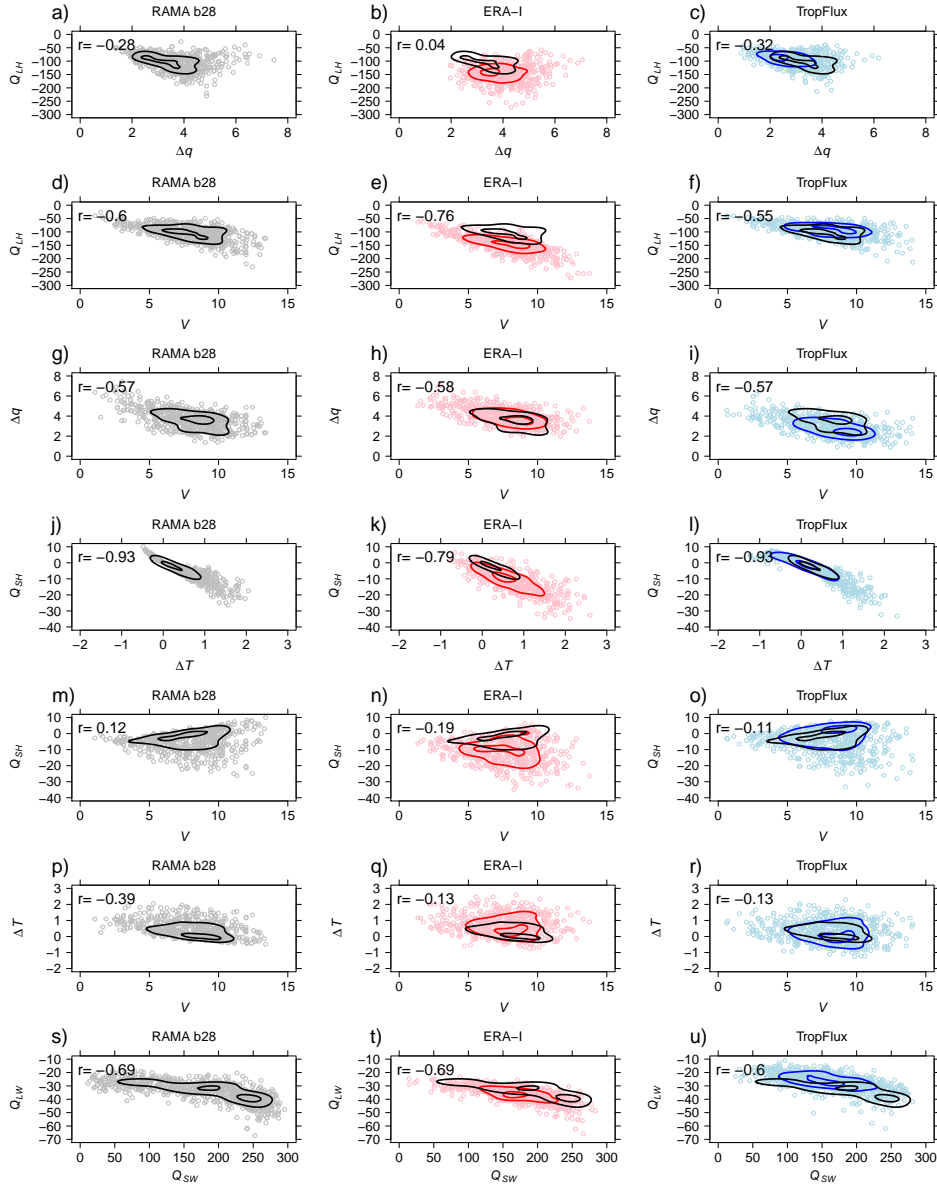
881 FIG. 1. Availability of data at buoy site b28 (15°N and 90°E b28) for meteorological and flux parameters
 882 used in this study.



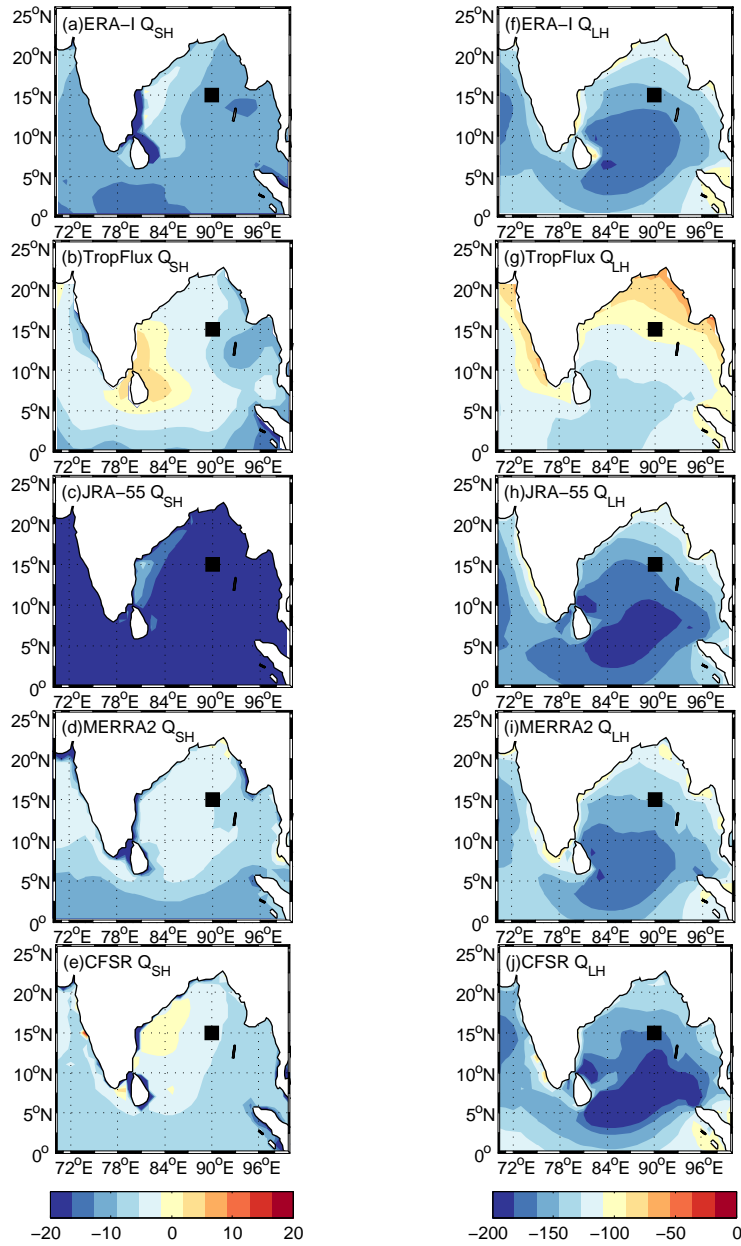
883 FIG. 2. Difference (product - RAMA; a), correlation (b), variance ratio (c), and skill score (d) for reanalysis
 884 products (ERA-I, TropFlux, JRA-55, MERRA-2 and CFSR) against data from RAMA b28. The 95% confidence
 885 intervals are shown in the difference, correlation and variance ratio metrics. The variables evaluated are the
 886 meteorological, SST ($^{\circ}C$), V ($m\ s^{-1}$), T_a ($^{\circ}C$), q_a ($g\ kg^{-1}$), ΔT ($^{\circ}C$), Δq ($g\ kg^{-1}$), and flux, Q_{SW} ($W\ m^{-2}$),
 887 Q_{LW} ($W\ m^{-2}$), Q_{SH} ($W\ m^{-2}$), Q_{LH} ($W\ m^{-2}$), Q_{net} ($W\ m^{-2}$), for the summer (JJAS) from 2007 to 2015. Panel
 888 (a) shows uncertainties as per Table 2 indicated by the horizontal dashed lines, and a split scale to differentiate
 889 between meteorological and flux parameters.



890 FIG. 3. Scatterplots for Q_{net} vs each of Q_{SW} , Q_{LW} , Q_{SH} and Q_{LH} (all units in $W m^{-2}$) from RAMA buoy
891 observations (a, b, c, d), ERA-I (e, f, g, h), TropFlux (i, j, k, l), JRA-55 (m, n, o, p), MERRA-2 (q, r, s, t) and
892 CFSR (u, v, w, x) at site b28 ($8^{\circ}N$ and $90^{\circ}E$). Contour lines enclose the 10% and 50% of points in each joint
893 distribution. RAMA contour lines (black) are repeated for comparison.



894 FIG. 4. Scatterplots of Q_{LH} (W m^{-2}) vs Δq (g kg^{-1}), Q_{LH} (W m^{-2}) vs V (m s^{-1}),
 895 Q_{SH} (W m^{-2}) vs ΔT ($^{\circ}\text{C}$), Q_{SH} (W m^{-2}) vs V (m s^{-1}), ΔT ($^{\circ}\text{C}$) vs V (m s^{-1}), and Q_{LW} (W m^{-2}) vs Q_{SW} (W m^{-2})
 896 from RAMA buoy observations (left column), ERA-Interim (center column) and TropFlux (right column) at site
 897 b28 (8°N and 90°E). Contour lines enclose the 10% and 50% of points in each joint distribution. RAMA contour
 898 lines (black) are repeated for comparison.



899 FIG. 5. Mean Q_{SH} (left column; $W m^{-2}$) and Q_{LH} (right column; $W m^{-2}$) for ERA-I (a, f), TropFlux (b, g),
 900 JRA-55 (c, h), MERRA-2 (d, i), and CFSR (e, j). All fields are averaged for the SW monsoon season (JJAS)
 901 from 2007 to 2015. The black square indicates the location of the RAMA buoy, b28, in the Bay of Bengal.

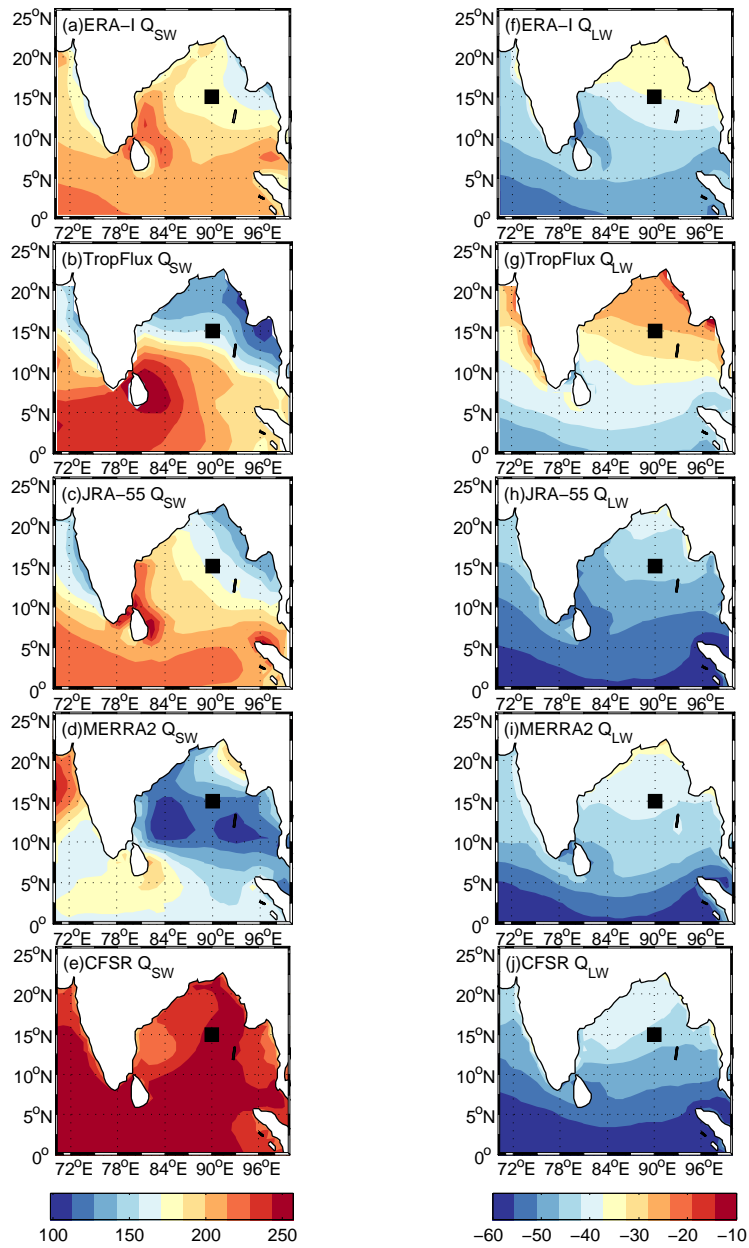
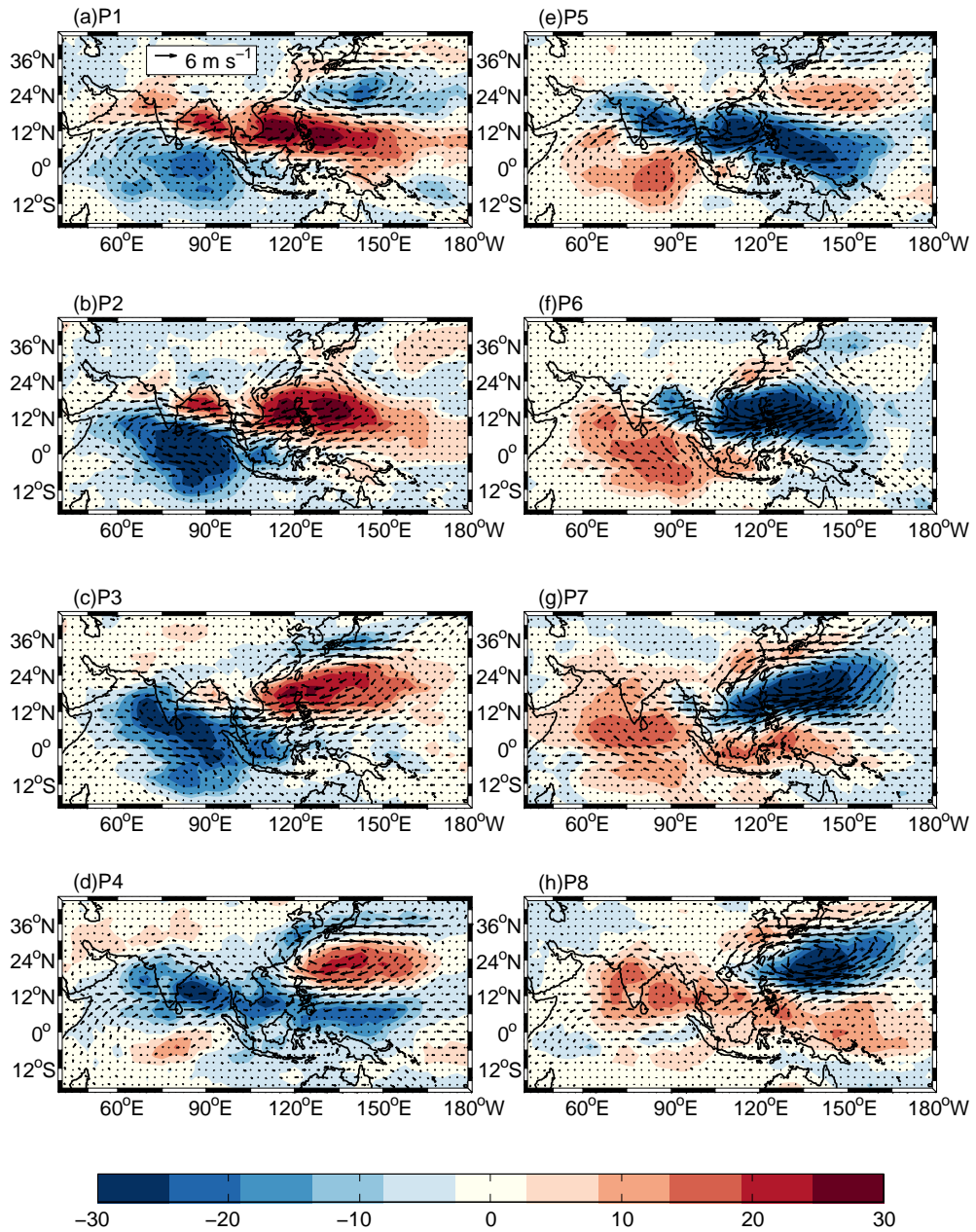
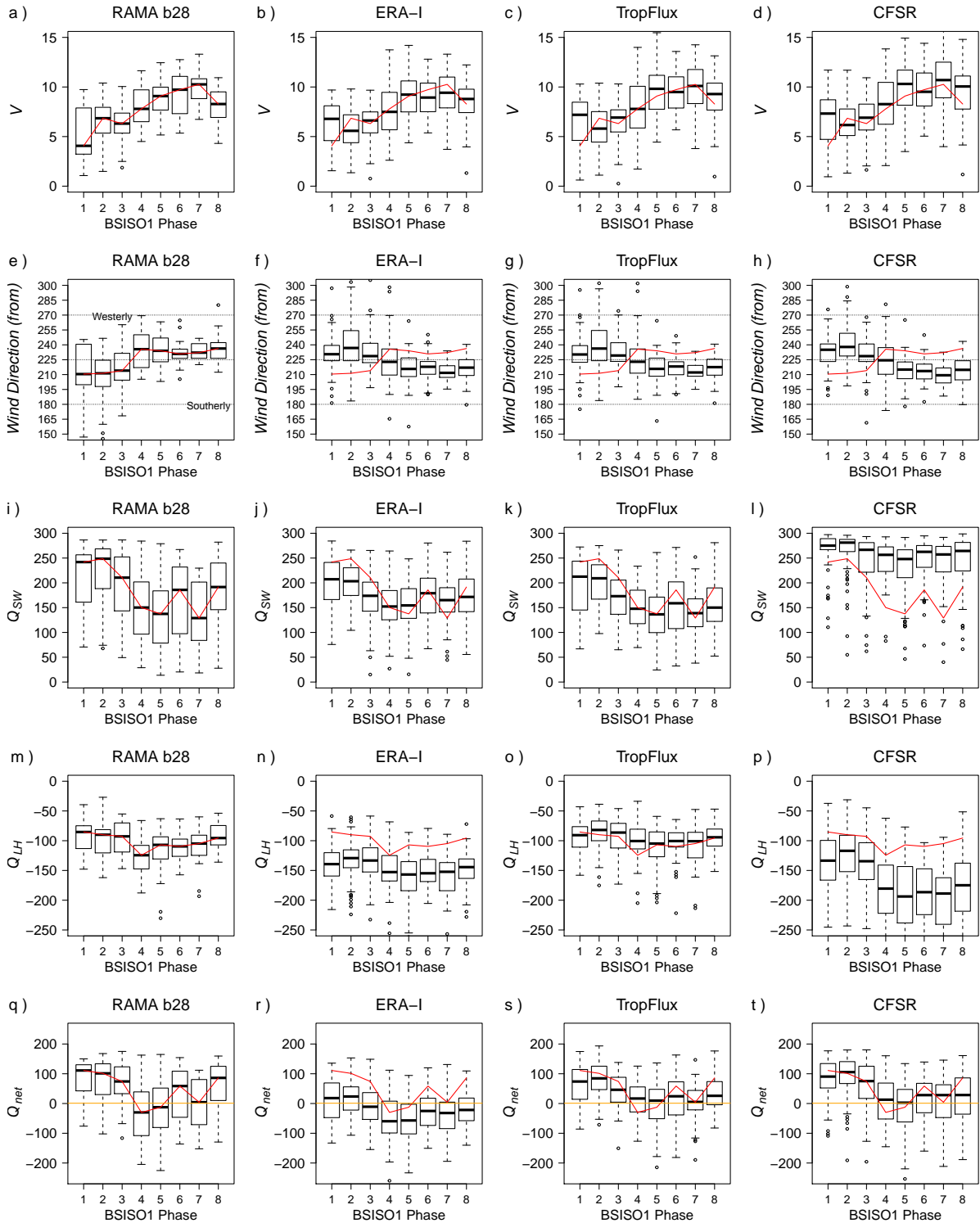


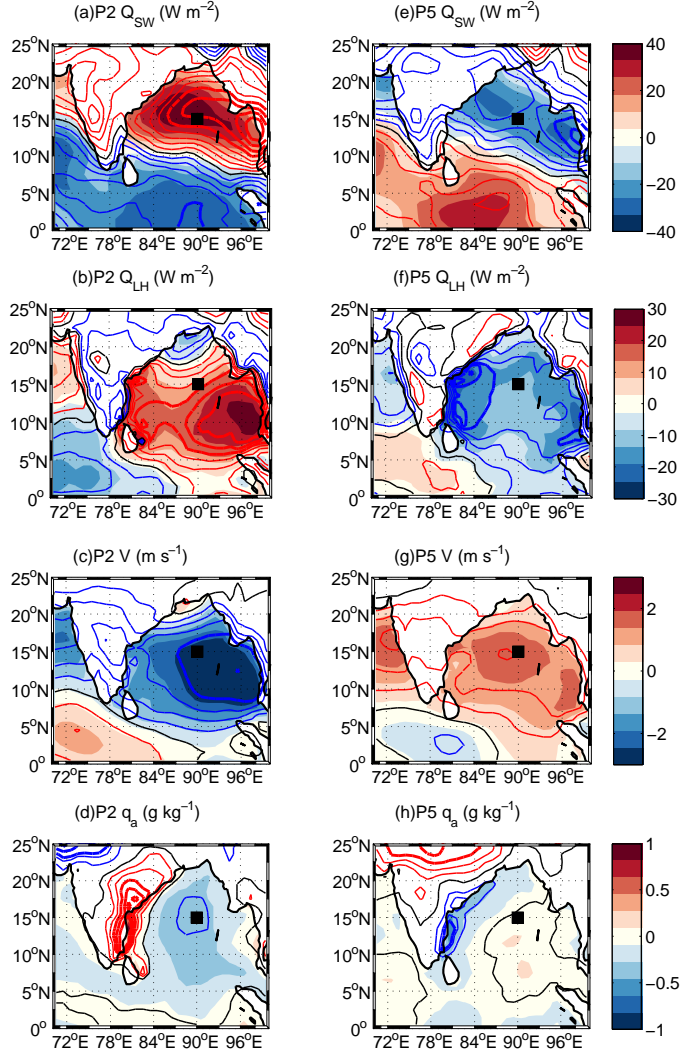
FIG. 6. Same as in Fig. 5 but for radiative fluxes.



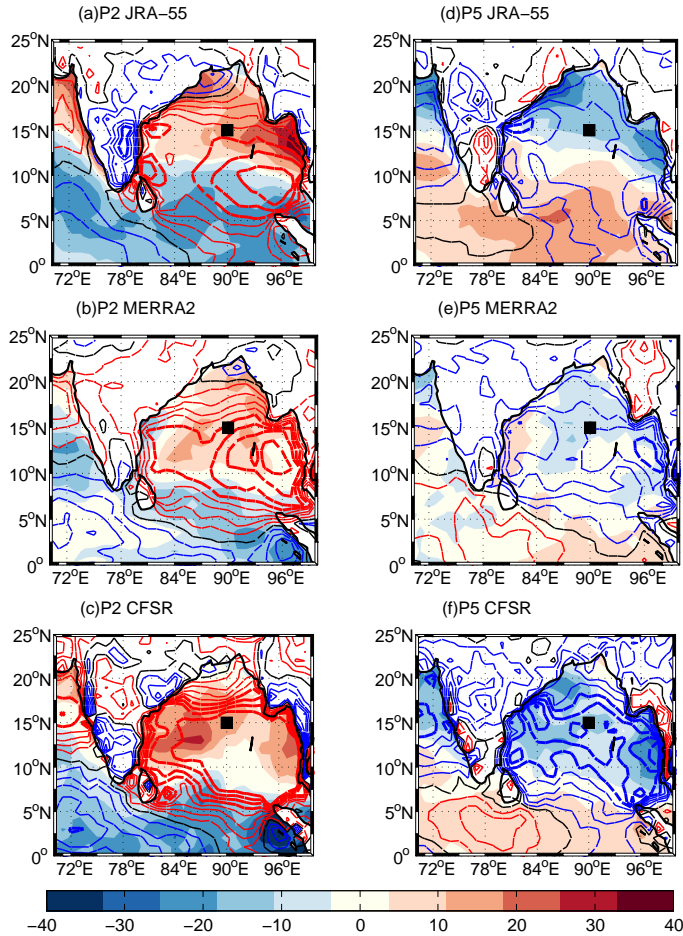
902 FIG. 7. BISO 1 life cycle composite of NOAA OLR anomalies (shaded; W m^{-2}) and NCEP-DOE 850-hPa
 903 wind anomalies (vector; m s^{-1}).



904 FIG. 8. Median, interquartile range, 95% confidence interval, and outliers for V (m s^{-1}),
 905 Q_{SW} (W m^{-2}), Q_{LH} (W m^{-2}), and Q_{net} (W m^{-2}) vs BSISO1 phases (1 to 8) from RAMA b28 (a, e, i, m, q),
 906 ERA-I (b, f, j, n, r), TropFlux (c, g, k, o, s), and CFSR (d, h, l, p, t). The red line is the RAMA b28 median line,
 907 repeated for comparison.



908 FIG. 9. Composite of phase 2 (left column) and phase 5 (right column) of the BSISO1 life cycle. TropFlux
 909 (shaded) and ERA-I (contour lines) Q_{SW} anomalies at phase 2 (a) and phase 5 (e); Q_{LH} anomalies at phase 2 (b)
 910 and 5 (f); V anomalies at phase 2 (c) and 5 (g); and, q_a anomalies at phase 2 (d) and 5 (h). ERA-I Q_{SW} contour
 911 lines range from -40 to 40 $W m^{-2}$ and Q_{LH} contour lines range from -30 to 30 $W m^{-2}$, with 5 $W m^{-2}$ intervals.
 912 ERA-I V contour lines range from -3 to 3 $m s^{-1}$, with 0.5 $m s^{-1}$ intervals. ERA-I q_a contour lines range from -1
 913 to 1 $g kg^{-1}$, with 0.2 $g kg^{-1}$ intervals. The black square indicates the location of the RAMA buoy 28.



914 FIG. 10. Phase 2 (left column) and 5 (right column) of the Q_{SW} (shading) and Q_{LH} (contour line) anomalies
 915 from JRA-55 (a, d), MERRA-2 (b, e), and CFSR (c, f) based on the BSISO1 phases. Q_{LH} contour lines range
 916 from -40 to 40 W m^{-2} , with 5 W m^{-2} intervals. The black square indicates the location of the RAMA buoy 28.
 917 All units in W m^{-2} .